CHEMISTRY OF MATERIALS

pubs.acs.org/cm

Article

Seeded Growth Combined with Cation Exchange for the Synthesis of Anisotropic $Cu_{2-x}S/ZnS$, $Cu_{2-x}S$, and $CuInS_2$ Nanorods

Chenghui Xia, Adrian Pedrazo-Tardajos, Da Wang, Johannes D. Meeldijk, Hans C. Gerritsen, Sara Bals, and Celso de Mello Donega*

Cite This: *Chem. Mater.* 2021, 33, 102−116

Read Online

ACCESS | Metrics & More | Article Recommendations | Supporting Information

ABSTRACT: Colloidal copper(I) sulfide ($Cu_{2-x}S$) nanocrystals (NCs) have attracted much attention for a wide range of applications because of their unique optoelectronic properties, driving scientists to explore the potential of using $Cu_{2-x}S$ NCs as seeds in the synthesis of heteronanocrystals to achieve new multifunctional materials. Herein, we developed a multistep synthesis strategy toward $Cu_{2-x}S/ZnS$ heteronanorods. The Janus-type $Cu_{2-x}S/ZnS$ heteronanorods are obtained by the injection of hexagonal high-chalcocite $Cu_{2-x}S$ seed NCs in a hot zinc oleate solution in the presence of suitable surfactants, 20 s after the injection of sulfur precursors. The $Cu_{2-x}S$ seed NCs undergo rapid aggregation and coalescence in the first few seconds after the injection, forming larger NCs that act as the effective seeds for heteronucleation and growth of ZnS. The ZnS heteronucleation occurs on a single (100) facet of the $Cu_{2-x}S$ seed NCs and is followed by fast anisotropic growth along a direction that is perpendicular to the *c*-axis, thus leading to $Cu_{2-x}S/ZnS$ Janus-type heteronanorods with a sharp heterointerface. Interestingly, the high-chalcocite crystal structure of the injected $Cu_{2-x}S$ seed NCs is preserved in the $Cu_{2-x}S$ segments of the heteronanorods because of the high-thermodynamic stability of this $Cu_{2-x}S$ phase. The $Cu_{2-x}S/ZnS$ heteronanorods are subsequently converted into single-component $Cu_{2-x}S$ and $CuInS_2$ nanorods by postsynthetic topotactic cation exchange. This work expands the possibilities for the rational synthesis of colloidal multicomponent heteronanorods by allowing the design principles of postsynthetic heteroepitaxial seeded growth and nanoscale cation exchange to be combined, yielding access to a plethora of multicomponent heteronanorods with diameters in the quantum confinement regime.

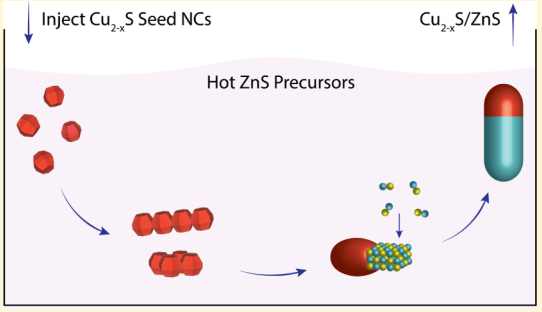

INTRODUCTION

Colloidal semiconductor heteronanocrystals (HNCs) exhibit unique optoelectronic properties that are inaccessible to single-component nanocrystals (NCs), making them promising materials for a wide range of applications such as light-emitting devices,[1,2] luminescent solar concentrators,[1,3] optoelectronic devices,[1,4] photocatalysis,[5,6] and biomedical imaging.[7−9] To date, numerous advances have been made in the liquid phase synthesis of various HNCs with controlled size, shape, and composition.[10−14] Most of the work to date has focused on Cd- or Pb-chalcogenide-based HNCs, which have reached a rather mature stage, leading to materials suitable for many applications (e.g., solar cells,[1,15,16] low-threshold lasing,[17] hydrogen evolution,[6] etc.). However, given the toxicity of Pb and Cd, the potential of these materials for large-scale applications is likely limited.

In contrast, copper(I) sulfide ($Cu_{2-x}S$) is a p-type semiconductor that is environmentally benign because it is based on nontoxic and abundant elements, while possessing composition-dependent band gaps and crystal structures (*viz.*, 1.1−1.4 eV for djurleite, x = 0−0.04; 1.5 eV for digenite, x = 0.2; 2.0 eV for covellite, x = 1).[18,19] These characteristics make $Cu_{2-x}S$ a promising candidate for high-performance photovoltaics in combination with n-type semiconductors (e.g., Cu_2S/In_2S_3[20]). In addition, the stoichiometry of $Cu_{2-x}S$ has been observed to have a great impact on the density of free holes, which increases with the increase of copper deficiency x, giving rise to localized surface plasmon resonances (LSPR) in the near-infrared (NIR) spectral range.[18,19] Control over the stoichiometry of $Cu_{2-x}S$ NCs therefore provides a useful tool not only to tailor the band gap and crystal structure of the material but also for achieving tunable absorption bands in the NIR by varying the free hole density. These remarkable features have driven scientists to explore synthesis routes toward $Cu_{2-x}S$-based HNCs to achieve new multifunctional materials for optoelectronic, photovoltaic, photocatalytic, and nanoplasmonic applications.[18,19,21,22]

Received: July 5, 2020
Revised: November 3, 2020
Published: December 28, 2020

$Cu_{2-x}S$/ZnS HNCs are particularly attractive because they are based only on nontoxic and abundant elements. Moreover, efficient photon-to-H_2 conversion has been reported for $Cu_{2-x}S$@ZnS nanocomposites under visible light,[23] implying the occurrence of charge separation, despite the type-I alignment between the bulk band potentials of the two materials. This has been attributed to photoinduced heterointerfacial charge-transfer transitions, through which a ZnS valence band electron is promoted directly to the conduction band of $Cu_{2-x}S$, creating a charge-separated state.[23] The optoelectronic properties of HNCs are determined not only by the band gap of its constituent materials and the band alignment between them (*viz.*, type-I, type-$I^{1/2}$, or type-II) but also by their morphology and heteroarchitecture.[10] Therefore, applications requiring efficient charge separation (e.g., photovoltaics and photocatalysis) greatly benefit from anisotropic morphologies, such as heterostructured nanorods [heteronanorods (HNR)].[24−28] The diameters of these HNRs should be sufficiently narrow to allow the use of quantum confinement effects to tailor the properties of 1-dimensional excitons. These prospects have motivated extensive research worldwide, which resulted in a variety of quantum confined HNR systems. Nevertheless, the best developed ones are still based on Cd-chalcogenides (e.g., CdSe/CdS dot-in-rod HNCs,[24−28] ZnSe/CdS dot-in-rod HNCs,[29] ZnSe−CdS−ZnSe dumbbell nanorods,[30] and double heterojunction CdSe−CdS−ZnS nanorods[31]), despite many important advances in recent years on the synthesis of $Cu_{2-x}S$-based HNCs.

Several synthetic strategies have been used in the quest for high-quality colloidal copper chalcogenide-based HNCs: (i) single-stage one-pot heating-up; (ii) multistage postsynthetic cation exchange; and (iii) multistage seeded growth. In the single-stage one-pot heating-up method, the HNCs are obtained by adding precursors of different components (either at once or sequentially) in the same reaction flask (e.g., $Cu_{2-x}S$/$CuInS_2$[32−35] and $Cu_{2-x}S$/ZnS HNRs[36,37]). Although this approach is appealing because of its simplicity, it offers limited control over the dimensions and heteroarchitecture of the product HNCs because of a number of unavoidable competing processes (e.g., formation of shells of mixed composition, homogeneous nucleation, etching, uncontrolled cation exchange, etc.).[10] Postsynthetic cation exchange reactions, in which cations ligated within a NC host lattice are replaced by guest cations from the solution, have recently been used to obtain copper chalcogenide-based (H)NCs that are not accessible by direct synthesis.[12,18,38−40] In particular, postsynthetic cation exchange methods have yielded HNCs of diverse composition, morphology, and heteroarchitecture, such as hamburger-like ZnS/$Cu_{2-x}S$/ZnS HNCs,[41] segmented $Cu_{2-x}S$/ZnS HNRs,[13,14] sculpted ZnS/$Cu_{1.8}S$ nanoplatelets,[13] sandwich-like $Cu_{2-x}S$−In_2S_3−ZnS HNCs,[42] CdSe/CdS−$Cu_{2-x}S$ dot core/rod shell HNRs,[43] and $CuInSe_2$/$CuInS_2$ dot core/rod shell HNRs.[44] The recent seminal work by Schaak and co-workers[14] is of particular interest because the authors developed a synthesis strategy based on multiple successive cation exchange steps starting on 20 nm diameter roxbyite $Cu_{1.8}S$ nanorods that led to the experimental demonstration of 113 different multicomponent axially segmented HNRs (up to 8 segments, made of up to 6 materials: $Cu_{2-x}S$, ZnS, $CuInS_2$, $CuGaS_2$, CoS, and CdS), and defined synthetic routes to 65,520 distinct multicomponent metal sulfide nanorods.

However, despite their astonishing versatility, cation exchange-based methods are inherently limited by the availability of suitable parent NCs, which act as templates in topotactic cation exchange reactions.[12,18] Therefore, the metal sulfide HNRs developed in the pioneer work by Schaak et al.[13,14] were nevertheless too large to allow quantum confinement effects to be exploited. This limitation is at present difficult to circumvent, given that the direct synthesis of quantum-confined Cu-chalcogenide nanorods is very challenging because reaction conditions that favor anisotropic growth typically lead to nanoplatelets, rather than nanorods, in striking contrast with NCs of II−VI semiconductors.[10,18,19] As a result, the currently available methods to directly synthesize colloidal $Cu_{2-x}S$ nanorods are limited to diameters larger than 10 nm,[32,33,45−48] which are larger than the exciton Bohr radius of $Cu_{2-x}S$ (3−5 nm[49]). $Cu_{2-x}S$ nanorods with diameters below 10 nm can at present only be obtained by Cd^{2+} for Cu^+ cation exchange in CdS nanorod templates.[50] This is a point of major concern, also regarding the synthesis of Cu-chalcogenide-based HNCs by cation exchange because many interesting quantum-confined Cu-chalcogenide HNRs have been obtained from Cd-chalcogenide HNC templates.[28,43,44] This is undesirable, given that it conflicts with one of the most appealing assets of Cu-chalcogenide-based nanomaterials (i.e., their nontoxic nature).

Postsynthetic seeded growth strategies have been instrumental in the development of colloidal Cd-chalcogenide HNCs and are responsible for the high degree of control and sophistication achieved over these nanomaterials.[10,24−28,30,31] The injection of NC seeds allows for a greater control over the formation of HNCs because it lowers the activation energy for heteronucleation of the second component of the HNC, thereby kinetically favoring heteroepitaxial growth and reducing the impact of undesired competing processes.[10,19,21,22] Further, the outcome of seeded growth reactions can be steered with precision by tailoring the characteristics of the injected seed NCs (composition, size, shape, and faceting), the surfactants present in the reaction medium, and the reaction conditions (temperature, concentrations of seed NCs and ligands, etc.).[10] Nevertheless, despite their proven success and versatility, seeded growth approaches have not been widely used in the synthesis of $Cu_{2-x}S$-based HNCs, with relatively few reports in the literature (e.g., rod-, teardrop- and matchstick-like Cu_2S/In_2S_3,[20] rod-like and dimeric $Cu_{2-x}S$/ZnS,[34,51−53] $Cu_{2-x}S$/$CuInS_2$,[34,54,55] and $Cu_{1.94}S$/$Zn_xCd_{1-x}S$[56,57] HNRs). Most of these $Cu_{2-x}S$-based HNCs have been obtained by injecting precursors of the second component into the suspension of $Cu_{2-x}S$ seed NCs. This makes the control of the size, shape, and composition of the product HNCs difficult because $Cu_{2-x}S$ NCs are very dynamic at elevated temperatures because of the high mobility of the Cu^+ ions in the NC lattice (diffusion coefficients are similar to those of liquids[58]), which is further enhanced in the presence of commonly used surfactants (e.g., alkylamines, oleic acid, and phosphines).[19] Moreover, the underlying growth mechanisms are still poorly understood, making the rational synthesis of $Cu_{2-x}S$-based HNCs with targeted compositions and morphologies challenging.

In this work, we developed a seeded growth approach to colloidal Janus-type $Cu_{2-x}S$/ZnS HNRs with diameters in the quantum confinement regime, which were not previously accessible either by direct synthesis or cation exchange-based approaches. The method is based on the injection of hexagonal high-chalcocite $Cu_{2-x}S$ NC seeds in a hot zinc oleate solution in the presence of suitable surfactants, 20 s after the injection of sulfur precursors. A previous work by our group on the synthesis of $CuInS_2$/ZnS HNRs has shown that the delay between the

https://dx.doi.org/10.1021/acs.chemmater.0c02817
Chem. Mater. 2021, 33, 102−116

injection of the sulfur precursor and the seed NCs allows the ZnS heteronucleation and heteroepitaxial growth rates to outpace competing processes and minimizes the impact of the thermal instability of the seed NCs.[59] Nonetheless, the $Cu_{2-x}S$ seed NCs undergo rapid aggregation and coalescence in the first few seconds after the injection, forming larger NCs that act as the effective seeds for heteronucleation and growth of ZnS. The ZnS heteronucleation occurs on a single (100) facet of the $Cu_{2-x}S$ seed NCs and is followed by fast anisotropic growth leading to $Cu_{2-x}S$/ZnS Janus-type HNRs with a sharp heterointerface. The crystal structure of the injected $Cu_{2-x}S$ seed NCs is preserved in the $Cu_{2-x}S$ segments of the HNRs, attesting the high-thermodynamic stability of the high-chalcocite phase under the conditions prevalent in our experiments. To demonstrate the suitability of the $Cu_{2-x}S$/ZnS HNRs as templates for cation exchange reactions, they are subsequently converted to $Cu_{2-x}S$ and $CuInS_2$ nanorods by topotactic cation exchange. This offers a new synthetic strategy to quantum-confined $Cu_{2-x}S$ and $CuInS_2$ nanorods and illustrates the versatility of our synthetic approach. The insights provided by our work allow the design principles of the postsynthetic heteroepitaxial seeded growth and nanoscale cation exchange to be combined, greatly expanding the scope of the rational synthesis strategies toward colloidal multicomponent HNRs with diameters in the quantum confinement regime.

EXPERIMENTAL SECTION

Materials. Copper(I) acetate (CuOAc, 97%), indium acetate [$In(Ac)_3$, 99.99%], zinc acetate (99.99%), tetrakis(acetonitrile)copper-(I) hexafluorophosphate ([$(CH_3CN)_4Cu]PF_6$, 97%), sulfur (S, 99.98%), trioctylphosphine oxide (TOPO, 99%), 1-dodecanethiol (DDT, 98%), trioctylphosphine (TOP, 90%), 1-octadecene (ODE, 90%), hexadecylamine (HDA, 90%), oleic acid (90%), nitric acid (HNO_3, 69.5%), anhydrous toluene, methanol, acetonitrile, and butanol were purchased from Sigma-Aldrich. Zinc oleate solution [$Zn(oleate)_2$, 0.25 mmol/g] was prepared according to the previously published procedures.[59] TOPO, ODE, and HDA were degassed at 120 °C overnight prior to synthesis. Other reagents were used as received. The chemicals were weighted and handled inside a glovebox.

Synthesis of $Cu_{2-x}S$ Seed NCs. The $Cu_{2-x}S$ seed NCs were synthesized according to previously reported procedures.[60,61] CuOAc (0.253 g, 2 mmol), TOPO (3.667 g, 9.3 mmol), and 20 mL of ODE were loaded in a 100 mL three-neck flask and degassed at 100 °C for 1 h. Then, the flask was purged by N_2 and the temperature was set to 210 °C. At 160 °C, 5 mL of DDT were swiftly injected into a flask. These NCs were allowed to grow at 210 °C for 40 min, followed by cooling down to room temperature. The crude products were mixed with isometric butanol and methanol, followed by centrifugation at 5000 rpm for 15 min. This washing step was repeated twice to remove residual precursors. The purified $Cu_{2-x}S$ NCs were dispersed into 20 mL of anhydrous toluene. The NC concentration (~2.25×10^{-5} M) was determined by inductively coupled plasma optical emission spectroscopy (ICP-OES) measurements (see Supporting Information, Method S1 for details).

$Cu_{2-x}S$/ZnS Colloidal HNRs. The $Cu_{2-x}S$/ZnS HNRs were synthesized by adapting a previously reported procedure.[59] In a typical synthesis, $Zn(oleate)_2$ (0.5 mmol), HDA (10 mmol), TOPO (10 mmol), and ODE (15 mL) were loaded into a 100 mL three-neck flask equipped with a condenser and degassed at 100 °C for 1 h. The flask was then purged by N_2 and heated to 210 °C. In the meantime, a stock solution of $Cu_{2-x}S$ seed NCs (6.525×10^{-5} M) was prepared by precipitating 1.45 mL of the preformed $Cu_{2-x}S$ NCs solution and redispersing into 500 μL of ODE. At 210 °C, 500 μL of the preheated S/TOPO solution (0.5 M) were rapidly injected into the flask. After 20 s, the 500 μL of $Cu_{2-x}S$ NCs were swiftly injected into the flask. This mixture was vigorously stirred at 210 °C for 10 min. The reaction was then quenched by injecting 10 mL of butanol. The resulting crude products were purified by using the same washing procedure described above. The purified $Cu_{2-x}S$/ZnS nanorods were dispersed into 10 mL of anhydrous toluene and stored in a glovebox. **Caution:** The quenching of the reaction by butanol must be done very carefully to avoid overflow of hot liquid and gases because the boiling point of butanol is much lower than the reaction temperature. It is advisable to always wear goggles while doing the experiments.

$Cu_{2-x}S$ Nanorods. The $Cu_{2-x}S$ nanorods were synthesized by full Zn^{2+} for Cu^+ cation exchange in $Cu_{2-x}S$/ZnS HNRs using a protocol adapted from the literature.[44,50] [$(CH_3CN)_4Cu]PF_6$ (32 mL, 0.0625 M) in anhydrous methanol were swiftly injected into 4 mL of the preformed $Cu_{2-x}S$/ZnS solution. The mixture was allowed to react for 30 min at room temperature in a glovebox. The products were collected by centrifugation at 2500 rpm for 15 min. The brown precipitates were further washed by adding 2 mL of toluene and 10 mL of methanol/butanol followed by centrifugation at 2500 rpm for 10 min. The $Cu_{2-x}S$ nanorod products were dispersed into a mixture of DDT (1 mL) and ODE (4 mL), and then kept under stirring at 100 °C for 3 h (this step is crucial to improve the stability of the $Cu_{2-x}S$ nanorods). The resulting products were washed 3 times using the same washing step mentioned above. The purified $Cu_{2-x}S$ nanorods were dispersed into 4 mL of anhydrous toluene.

$CuInS_2$ Nanorods. The $CuInS_2$ nanorods were synthesized by partial Cu^+ for In^{3+} cation exchange in $Cu_{2-x}S$ nanorods following previously published procedures.[61] The preformed $Cu_{2-x}S$ nanorod solution (2 mL) was degassed to remove toluene and then dispersed into 500 μL of DDT and 4.5 mL of predegassed ODE. Meanwhile, a mixture of $In(Ac)_3$ (1 mmol), TOP (500 μL), and ODE (4.5 mL) was heated to 120 °C. Then, ~5 mL of the $Cu_{2-x}S$ nanorod solution was added into the hot indium complex solution. To ensure exchange, the mixture was kept at 120 °C overnight. The product $CuInS_2$ nanorods were washed 3 times using the same washing procedure described above. The purified $CuInS_2$ nanorods were dispersed into 2 mL of anhydrous toluene.

Optical Spectroscopy. Samples for optical measurements were prepared by dispersing the NCs into 3 mL of anhydrous toluene in 10 mm path length sealed quartz cuvettes. Absorption spectra were recorded on a double-beam PerkinElmer Lambda 950 UV/vis/NIR spectrometer.

X-ray Diffraction. X-ray diffraction (XRD) patterns were recorded on a Bruker D2 PHASER, equipped with a Co Kα X-ray source (1.79026 Å). Samples were washed at least 3 times, dried under vacuum overnight, and uniformly dispersed on a silicon wafer prior to the XRD measurements.

Inductively Coupled Plasma Optical Emission Spectroscopy. ICP-OES measurements were performed on a PerkinElmer Optima 8300 ICP-OES spectrometer equipped with a high-performance segmented-array charge-coupled device detector. Samples were carefully dried under vacuum overnight and thoroughly dissolved in HNO_3 (69%). The digested samples were further diluted 1000 times to reach <1 ppm range for the measurements. The relative standard deviation of Cu (at 327.393 nm), In (at 230.606 nm), and Zn (at 206.200 nm) is less than 1%.

Transmission Electron Microscopy. The samples were diluted and dropcasted on ultra-thin copper or aluminum grids. Conventional transmission electron microscopy (TEM) images were acquired using a Thermo Fisher Scientific Tecnai-20 microscope operating at 200 kV. High-resolution TEM (HRTEM), high-angle annular dark field-scanning TEM (HAADF-STEM), and elemental mapping were performed on a Talos F200X (Thermo Fisher Scientific) operated at 200 kV. The analysis of HRTEM images was performed using a Crystallographic Tool Box software (CrysTBox).[62,63] This software can automatically determine the zone axis from a diffraction pattern, assign crystallographic indices to the diffraction spots, and measure the interplanar distances. The measured *d*-spacings and interplanar angles are paired with the expected values based on the crystal structure standards. Only assignments that fulfill certain physical and crystallographic constraints are taken into account. The elemental mapping results were acquired in an area of 1024 × 1024 pixels with an

https://dx.doi.org/10.1021/acs.chemmater.0c02817
Chem. Mater. 2021, 33, 102−116

acquisition time of 5 min using Esprit software from Bruker. The elemental quantification from the mapping is done by adding up all the counts in the entire spectrum for each channel and all pixels within the area of interest. Additionally, elemental line scans were performed by scanning the electron beam over a predefined line across the NCs and quantifying the NC composition as described above on 100 spots selected along the scanned line. High-resolution HAADF-STEM images were acquired using a cubed Thermo Fisher Scientific Titan microscope operating at 300 kV.

Electron Tomography. Three microliters of diluted HNC dispersion was dropcasted on a graphene grid. Electron tomography was performed on a Thermo-Fisher Osiris electron microscope operated at 80 kV in HAADF-STEM mode. The tilt series were acquired manually within a tilt range from −70 to +65° and an increment of 5°. A convolutional neural network was used to restore individual HAADF-STEM images.[64] The corrected images were then aligned based on phase correlation. 3D reconstruction was performed by a novel approach consisting of iterating between 50 simultaneous iterative reconstruction technique (SIRT) cycles and application of constraints in the real and Fourier space.[64] After applying a bandwidth limit to the fast Fourier transform, the result is transformed to real space and a threshold is applied to the intensity of the 3D volume. Next, the SIRT cycles are repeated.

***In Situ* Heating TEM.** *In situ* heating TEM experiments were performed using a cubed Thermo Fisher Scientific Titan microscope operating at 300 kV in HAADF-STEM mode using a DENSsolution Wildfire tomography heating holder. Diluted HNC dispersion (3 μL) was dropcasted on a Wildfire nanochip. The sample was heated without electron-beam illumination from 25 to 210 °C at a rate of 15 °C/min. After 5 min stabilization, HAADF-STEM images were acquired. Subsequently, the sample was heated from 210 to 240 °C with the same heating rate and stabilized for 5 min before acquiring HAADF-STEM images.

RESULTS AND DISCUSSION

Colloidal $Cu_{2-x}S$/ZnS HNCs. Figure 1a schematically depicts the procedure used to synthesize $Cu_{2-x}S$/ZnS HNCs *via* a seeded growth approach adapted from a previous work.[59] In a typical synthesis, ∼5.3 nm dodecanethiol-capped $Cu_{2-x}S$ NCs (500 μL, 6.525×10^{-5} M) were injected in a hot solution of zinc oleate, TOPO, and HDA in octadecene, 20 s after the injection of 500 μL of sulfur/TOPO (S/TOPO, 0.5 M) at 210 °C (Figure 1a, see Experimental Section for details). The reaction solution was kept at this temperature for 10 min. TEM shows that the product NCs possess rod-like shapes with an average diameter of 6.2 ± 0.7 nm and a length of 17.8 ± 1.2 nm (Figure 1c). The XRD pattern of the $Cu_{2-x}S$ seed NCs can be assigned to the hexagonal high-chalcocite Cu_2S crystal structure (Figure 1d).[59,61] The XRD pattern of the product nanorods is dominated by peaks that can be unambiguously ascribed to wurtzite ZnS with several extra peaks at 43.9 and ∼64.5° (Figure 1d, Supporting Information Figure S1). The peak at 43.9° matches well the (102) diffraction peak of the hexagonal high-chalcocite Cu_2S phase, while the very weak peaks at ∼64.5° are consistent with diffraction by the (112), (004), and (201) planes of the hexagonal high-chalcocite Cu_2S. Moreover, the peak at 55.9°, assigned to the (110) plane of hexagonal wurtzite ZnS, shows additional shoulders that are likely due to contributions by the (110) and (103) planes of hexagonal high-chalcocite Cu_2S. This structural assignment is confirmed by HRTEM studies, which will be discussed in detail later in this work. The XRD pattern of the product nanorods thus indicates that they consist of wurtzite ZnS and high-chalcocite $Cu_{2-x}S$ domains, that is, they are $Cu_{2-x}S$/ZnS HNCs.

It is also clear that the volume fraction of ZnS in the product HNCs is larger than that of $Cu_{2-x}S$ because the diffraction peaks

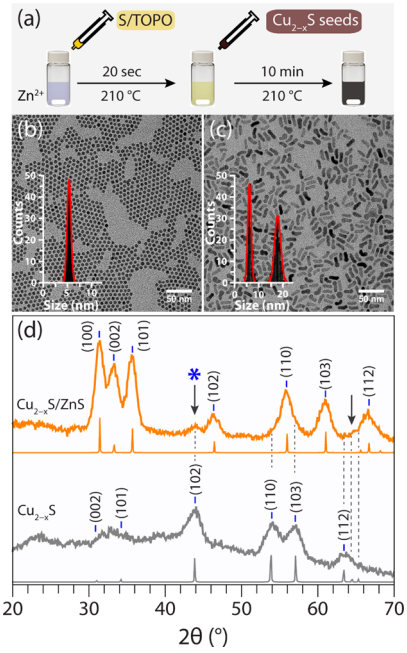

Figure 1. (a) Synthesis scheme of $Cu_{2-x}S$/ZnS HNCs *via* a seeded growth approach. Zn^{2+} represents a mixture of zinc oleate, TOPO, and HDA in octadecene. (b,c) TEM images and corresponding size histograms of $Cu_{2-x}S$ seed NCs [(b), diameter: 5.3 ± 0.4 nm] and $Cu_{2-x}S$/ZnS HNCs [(c), diameter: 6.2 ± 0.7 nm; length: 17.8 ± 1.2 nm]. The size distribution histograms are constructed by measuring over 200 NCs and are fitted to Gaussian functions. (d) XRD patterns of the $Cu_{2-x}S$ seed NCs (grey line) and the product $Cu_{2-x}S$/ZnS HNCs (orange line). The sharp grey lines represent the hexagonal high-chalcocite Cu_2S diffraction pattern (JCPDS Card 00-026-1116). The sharp orange lines represent the hexagonal wurtzite ZnS diffraction pattern (JCPDS card 01-084-3995). The dashed lines and black arrows indicate the diffraction peaks assigned to hexagonal high-chalcocite Cu_2S NCs in the product HNCs. The most pronounced diffraction peak of Cu_2S in the XRD pattern of the HNCs (43.9°) is also marked by a blue asterisk. Multi-Gaussian peak fits of the XRD patterns and corresponding crystallite sizes are given in Figure S1 and Table S1 in the Supporting Information.

of wurtzite ZnS dominate the XRD pattern (Figure 1d, Supporting Information Figure S1). To assess the crystallinity and dimensions of the $Cu_{2-x}S$ seed NCs and of the $Cu_{2-x}S$ and ZnS domains of the product $Cu_{2-x}S$/ZnS HNCs, crystallite sizes were estimated from the XRD patterns using Scherrer's equation (Supporting Information, Figure S1 and Table S1). For the ZnS domain, the crystallite size, estimated by averaging the values obtained from all seven diffraction peaks observed in the XRD pattern, is 6.4 ± 0.8 nm, which is in excellent agreement with the diameter of the product nanorods estimated from the TEM images (Figure 1c). As the (102) diffraction peak of hexagonal high-chalcocite Cu_2S is observed in the XRD patterns of both the $Cu_{2-x}S$ seed NCs and the product nanorods, this peak was used to estimate the $Cu_{2-x}S$ crystallite sizes. It was found that the crystallite sizes of the $Cu_{2-x}S$ seed NCs and the $Cu_{2-x}S$ domains in the HNCs are ∼5.4 and ∼6.3 nm, respectively. These values are consistent with the diameters extracted from the TEM images for the seed NCs and product nanorods, respectively (Figure 1b,c). This analysis shows that the diameter of the ZnS and $Cu_{2-x}S$ domains of the HNCs are similar, implying that the HNCs are axially segmented $Cu_{2-x}S$/ZnS HNRs and suggesting that the size of the seed NCs was not preserved in the $Cu_{2-x}S$ segments of the product HNCs. Given that Scherrer's crystallite

https://dx.doi.org/10.1021/acs.chemmater.0c02817
Chem. Mater. 2021, 33, 102−116

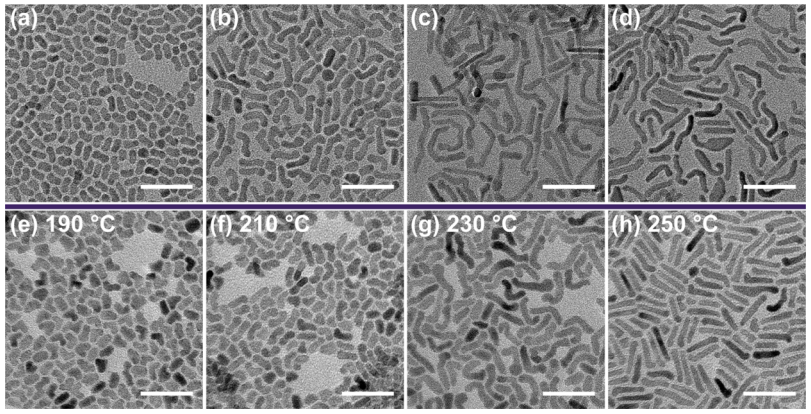

Figure 2. (a–d) TEM images of $Cu_{2-x}S$/ZnS HNCs synthesized by injecting $Cu_{2-x}S$ NCs in a hot solution of zinc oleate and TOPO and HDA in octadecene, 20 s after the injection of S/TOPO, using an increasing concentration of ZnS precursors [from (a–d)]. The reaction was allowed to proceed at 210 °C for 10 min. Scale bars are 50 nm. (e–h) TEM images of $Cu_{2-x}S$/ZnS HNCs synthesized by injecting $Cu_{2-x}S$ NCs in a hot solution of zinc oleate and TOPO and HDA in octadecene, 20 s after the injection of S/TOPO, at different reaction temperatures. The concentration of ZnS precursors is the same as that used to prepare the samples shown in panel (b). Scale bars are 50 nm.

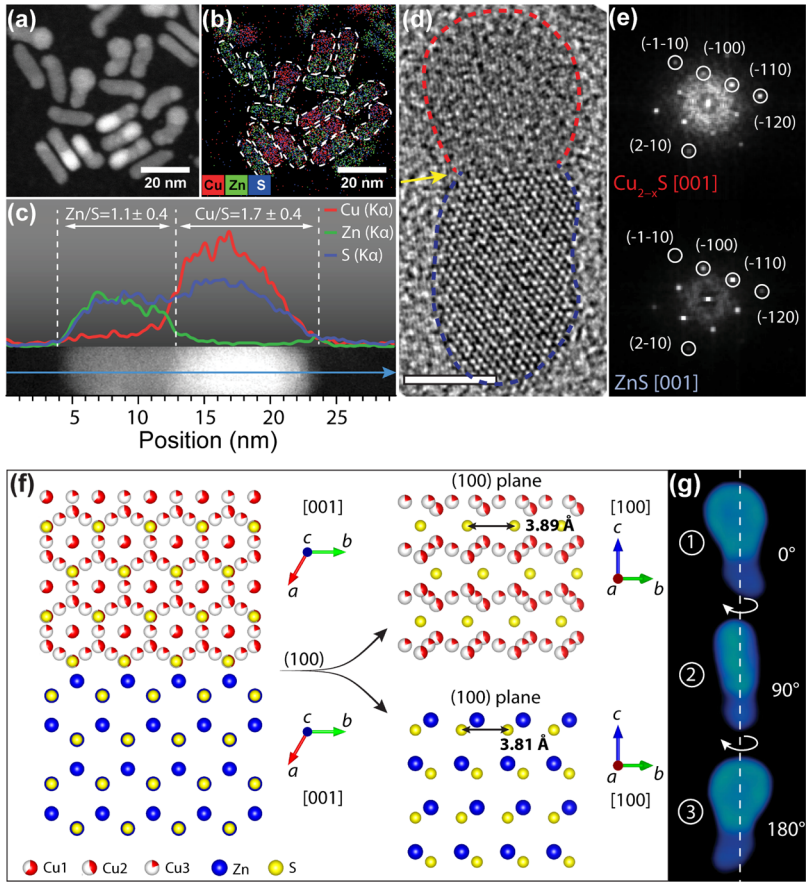

Figure 3. (a,b) HAADF-STEM image (a) and corresponding elemental mapping (b) of $Cu_{2-x}S$/ZnS HNCs. (c) Elemental line scan of a single $Cu_{2-x}S$/ZnS HNC (atomic ratios: Zn/S = 1.1 ± 0.4; Cu/S = 1.7 ± 0.4). The blue arrow in the lower panel indicates the scanned line. Elemental quantification was performed on 100 spots along this line. (d) HRTEM image of a single $Cu_{2-x}S$/ZnS HNC. A yellow arrow indicates the heterointerface between $Cu_{2-x}S$ (red dashed contour line) and ZnS (blue dashed contour line). Scale bar is 5 nm. (e) FT patterns of $Cu_{2-x}S$ part (upper panel) and ZnS part (lower panel). The FT patterns can be indexed to the axial projection of the high-chalcocite Cu_2S and the wurtzite ZnS structures along the [001] direction, respectively. (f) Schematic model for the atomic arrangement of the epitaxial growth of hexagonal wurtzite ZnS onto the (100) plane of hexagonal high-chalcocite Cu_2S through its (100) plane, viewed along the [001] direction. The atomic models of the (100) plane of Cu_2S and the (100) plane of ZnS are displayed on the right side. (g) Reconstructed 3D model of a single $Cu_{2-x}S$/ZnS HNC displaying a pronounced inter-NC contrast difference, similar to those in the lower left side of panel (a) [not the same HNC shown in panel (d)]. Images 2 and 3 correspond to image 1 rotated by 90 and 180°, respectively. $Cu_{2-x}S$ is represented in cyan, while blue represents ZnS. An animated (rotating) version of this model is provided in the Supporting Information.

https://dx.doi.org/10.1021/acs.chemmater.0c02817
Chem. Mater. 2021, 33, 102–116

sizes reflect the smaller dimension of the crystallites and are not sensitive to the total scattering volume and that low-resolution TEM images, such as the one shown in Figure 1b, do not allow a clear distinction between the $Cu_{2-x}S$ and ZnS segments of the HNCs, these inferences can only be confirmed by HRTEM studies, which will be discussed in detail in the next section after additional experiments on the formation of the $Cu_{2-x}S$/ZnS HNCs are presented.

Control experiments performed without injection of the $Cu_{2-x}S$ NC seeds, while keeping all other parameters unchanged, yielded only very small ZnS NCs (Supporting Information, Figure S2). This demonstrates that the product, $Cu_{2-x}S$/ZnS HNCs, is formed by a seeded growth mechanism. To understand the formation of the $Cu_{2-x}S$/ZnS HNCs, the influence of the sulfur sources, ZnS precursor concentration, reaction time, and reaction temperature was investigated. The use of elemental sulfur dissolved in TOPO (S/TOPO) as the S-source instead of other common S-precursors, such as dodecanethiol, sulfur in octadecene, sulfur in TOP, and sulfur in oleylamine, effectively promotes the formation of nanorods (Supporting Information, Figure S3). We therefore use S/TOPO as the S-precursor in the subsequent studies unless otherwise noted. The morphology of the product $Cu_{2-x}S$/ZnS HNCs is greatly affected by the TOPO concentration in the HDA-activated zinc oleate solution, with equimolar amounts of TOPO and HDA yielding straighter and better defined nanorods (Supporting Information, Figure S4). We thus use an equimolar mixture of TOPO and HDA as surfactants to study the influence of the ZnS precursor concentration on the formation of $Cu_{2-x}S$/ZnS HNCs. As shown in Figure 2a–d, the aspect ratio of the product $Cu_{2-x}S$/ZnS HNCs can be varied by controlling the concentration of ZnS precursors. The product HNCs, however, display significant deviations from the ideal linear nanorod shape, especially in the case of the high concentration of ZnS precursors (Figure 2a–d). The growth rate of the $Cu_{2-x}S$/ZnS HNCs is rather slow (~1.3 nm/min, 210 °C) in comparison with that previously reported for $CuInS_2$/ZnS (~21 nm/min, 210 °C)[59] and CdSe/CdS (~19 nm/min, 350 °C)[65] dot-in-rod HNCs (Supporting Information, Figure S5). The aspect ratio of the $Cu_{2-x}S$/ZnS HNCs could be tuned by adjusting the reaction temperature. Higher reaction temperatures promote the growth of longer and straighter nanorods (Figure 2e–h). However, too high temperatures (250 °C) lead to the formation of many isolated small NCs, which coexist with the nanorods (Supporting Information, Figure S6). These NCs are likely homogenously nucleated ZnS NCs because alkylamines can activate zinc carboxylate precursors, thereby promoting the formation of ZnS at elevated temperatures (over 200 °C).[66] A possible mechanism for the formation and growth of $Cu_{2-x}S$/ZnS HNCs is discussed in more detail after the structural characterization section below.

Structural Characterization of Colloidal $Cu_{2-x}S$/ZnS HNCs. HAADF-STEM images of $Cu_{2-x}S$/ZnS HNCs show pronounced contrast differences within single HNCs (Figure 3a, Supporting Information Figure S7). Two-dimensional elemental mapping (Figure 3b) reveals that this contrast difference may be because of differences in atomic number because brighter segments of the HNCs are observed to correspond to Cu_2S (average *Z*-number: 24.7) while the darker ones correspond to ZnS (average *Z*-number: 23). However, as will be discussed in more detail below, the contrast differences observed within single HNCs also originate from differences in the thickness of the two segments.

An elemental line scan through a single HNC gives quantitative information on the spatial distribution of each constituent element (Figure 3c). The copper sulfide segment is $Cu_{1.7\pm0.4}S$, while the zinc sulfide segment is $Zn_{1.1\pm0.4}S$. The product $Cu_{2-x}S$/ZnS HNCs show a broad and weak NIR absorption band (Supporting Information, Figure S8). An absorption band in the NIR is often observed in Cu-chalcogenide NCs and is ascribed to LSPR because of excess free holes in the valence band (i.e., p-doping), which originate from Cu^+ vacancies.[18,19,21,59,67] The intensity of the LSPR absorption band increases with the density of free holes, which is in turn dependent on the degree of Cu-deficiency of the $Cu_{2-x}S$ NC (i.e., on the value of x).[18,19] The observation of a weak NIR absorption band in the spectra of the product $Cu_{2-x}S$/ZnS HNCs thus implies that the density of free holes (and thus the concentration of Cu vacancies) in the $Cu_{2-x}S$ segments is low, consistent with the observed crystal structure (x for high-chalcocite $Cu_{2-x}S$ is typically smaller than 0.03).[17] HRTEM images and corresponding Fourier Transform (FT) patterns of single nanoparticles show that the $Cu_{2-x}S$/ZnS HNCs are crystalline and consist of hexagonal high-chalcocite Cu_2S and hexagonal wurtzite ZnS domains connected through a sharp heterointerface, irrespective of the $Cu_{2-x}S$ and ZnS volume fractions in the HNCs (Figure 3d,e, and Supporting Information Figures S9 and S10 and Tables S2, S3 and S4). We note that this corroborates the structural assignments based on the analysis of the ensemble XRD patterns (Figure 1) and absorption spectra (Figure S8) (see above). The hexagonal wurtzite ZnS segment coherently attaches to the (100) plane of hexagonal high-chalcocite Cu_2S through its (100) plane and heteroepitaxially grows along the ⟨100⟩ direction that is perpendicular to the *c*-axis (see Supporting Information, Figure S9 and Tables S2 and S3 for details). Similar results were obtained from the analysis of several other $Cu_{2-x}S$/ZnS HNCs, covering a wide range of HNC architectures and compositions ($Cu_{2-x}S$ volume fractions from ~0.2 to ~0.8), including both dominant and minority HNC types (Supporting Information, Figure S10 and Table S4). Figure 3f depicts the atomic arrangement of the heteroepitaxial overgrowth of ZnS onto the $Cu_{2-x}S$ seed NCs. The epitaxial (100) heterointerfaces between the two materials show well-matched sulfur sublattices shared by hexagonal high-chalcocite Cu_2S (space group $P6_3/mmc$) and hexagonal wurtzite ZnS ($P63/mc$) with a small lattice mismatch of 2.1%. Moreover, as observed in several other $Cu_{2-x}S$/ZnS HNCs (Supporting Information, Figure S10), the heteroepitaxial growth also occurs on the (−100) planes of $Cu_{2-x}S$ seed NCs, which is likely due to the similar atomic arrangements of the (100) and (−100) planes of the high-chalcocite Cu_2S structure, leading to similar $Cu_{2-x}S$/ZnS heterointerfaces with a small lattice mismatch of 2.1%. As proposed by Schaak and co-workers,[13,14] the lattice mismatch can be used as a proxy for heterointerfacial strain, implying that interfaces with the smallest mismatches are preferred because they yield the smallest strain fields. It is interesting to note that the phase of the $Cu_{2-x}S$ seed NCs (hexagonal high-chalcocite) is preserved in the $Cu_{2-x}S$ segment of the single $Cu_{2-x}S$/ZnS HNCs, regardless of the $Cu_{2-x}S$ volume fraction and the facet onto which ZnS grows, that is, (100) or (−100). The significance of these observations will be discussed in detail below, in the Growth Mechanism section.

To further elucidate the origin of the pronounced contrast differences observed within some of the HNCs (see e.g., lower left side of Figure 3a), electron tomography was performed to reconstruct the shape of single $Cu_{2-x}S$/ZnS HNCs (Figure 3g).

https://dx.doi.org/10.1021/acs.chemmater.0c02817
Chem. Mater. 2021, 33, 102−116

By rotating the viewing direction, we observe that the $Cu_{2-x}S$ domain has a disk shape (aspect ratio ~2), while the ZnS grows only on one of its side facets. The pronounced interparticle contrast observed within this HNC can thus be attributed to the thickness difference of the $Cu_{2-x}S$ and ZnS segments when the HNC is oriented with the wider side of the $Cu_{2-x}S$ nanodisk perpendicular to the TEM grid. This is consistent with the observation of neighboring HNCs clearly consisting of a $Cu_{2-x}S$ nanodisk with a ZnS rod attached to one of its sides [see, e.g., the HNC near the center of panel (a) of Figure 3]. The inter-HNC contrast observed in the HAADF-STEM images is thus caused by differences in both the composition and thickness of the different segments of the HNC (Figures 3a−c and S7). It should be noted that the HNC shown in Figure 3g is however not typical because its $Cu_{2-x}S$ volume fraction is larger than that of ZnS, in contrast with the majority of the $Cu_{2-x}S$/ZnS HNCs (see Figures 1, 3, S2, S7, S9, and S10). Nevertheless, it is striking that in all cases the $Cu_{2-x}S$ segments of the HNCs are larger than the Cu_2S seed NCs injected in the reaction mixture. The sizes of the $Cu_{2-x}S$ segments can be estimated based on the differences in contrast (Figures 3a,c, and S7), elemental distribution (Figure 3b), and HRTEM images (Figures 3d and S10) of single HNCs. It is found that the size of the $Cu_{2-x}S$ segments ranges from 5.5 to ~12 nm (average: 8.4 ± 1.4 nm, Supporting Information, Figure S11), which is larger than the size of the injected seed NCs (5.3 ± 0.4 nm). The average volume of the $Cu_{2-x}S$ segments can be roughly estimated by assuming them to be either nanodisks or nanorods, as evidenced by the HAADF-STEM and HRTEM images (Figures 3, S7 and S10). The average dimensions obtained in Figure S11 can then be interpreted as either the length of nanorods with a diameter equal to 5.5 nm, yielding an average volume of ~2.6V_0 (V_0 = initial volume of injected $Cu_{2-x}S$ seed NCs), or the diameter of nanodisks with thickness equal to 5.5 nm, yielding an average volume of ~3.9V_0. This estimate indicates that the volume of the $Cu_{2-x}S$ segments is ~3−4 times larger than that of the initially injected $Cu_{2-x}S$ seed NCs. The implications of this observation will be discussed in the Mechanism section below.

Growth Mechanism of Colloidal $Cu_{2-x}S$/ZnS HNCs. To gain insights into the formation of the $Cu_{2-x}S$/ZnS HNCs, we analyzed aliquots of the seeded growth reaction from the early stage to the end of reaction by *ex situ* TEM (Supporting Information Figure S5). We observe that 5 s after the injection, NCs with the original size are virtually absent and the majority of the NCs already has sizes of ~7 nm (~55%) and ~9 nm (~30%), with smaller fractions with even larger sizes (11, 13, and 15 nm). This rapid increase in size is accompanied by the appearance of a few NCs with elongated or distorted shapes, although the majority still appears nearly spherical. After 1 min, the fraction of NCs with larger sizes has increased, but the size increase is mostly because of the elongation of the NCs, which now consist mostly of distorted nanorods. The fraction of NCs with sizes in the 10−16 nm range continues to increase over the next 4 min, with a concomitant increase in the shape polydispersity. Further progress of the reaction leads to the reduction of the shape polydispersity, accompanied by an increase of the average length and a slight reduction of the average diameter. We note that the average size of the NCs after 5 s (7.8 ± 1.1 nm) is already close to the average final size of the $Cu_{2-x}S$ segments of the HNCs (~8.4 ± 1.4 nm, see above), suggesting that the rapid increase in size is primarily because of the growth of the $Cu_{2-x}S$ seed NCs themselves. Considering that NCs with sizes smaller than the original size of the injected seed NCs are absent, we surmise that the contribution of Ostwald ripening is not significant.[68] The rapid increase in size at the early stages of the reaction is thus ascribed to the coalescence of the original seed NCs into larger $Cu_{2-x}S$ NCs, which then act as seeds for the heteronucleation and growth of ZnS. The heteroepitaxial growth is also fast because most of the increase in size occurs in the first minute. After that, a phase of slower heteroepitaxial growth, accompanied by internal ripening, is entered. The final few minutes of the reaction seem to consist primarily of internal ripening and reconstruction. This mechanism is schematically depicted in Figure 4 and will be discussed in more detail below.

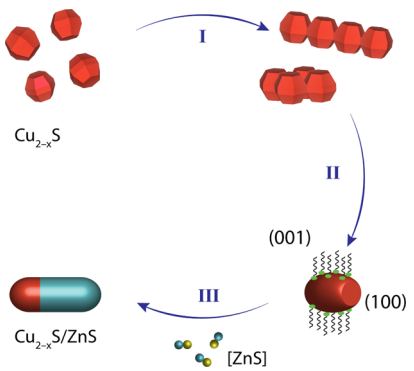

Figure 4. Schematic illustration of the mechanism proposed for the multistep seeded growth protocol used in this work to synthesize colloidal $Cu_{2-x}S$/ZnS HNRs.

The observation of coalescence implies that the seed NCs are very dynamic at the reaction temperature. To evaluate the thermal stability of the $Cu_{2-x}S$ seed NCs, *in situ* heating TEM measurements were carried out. These experiments show that the $Cu_{2-x}S$ seed NCs are extremely dynamic and undergo widespread ripening, coalescence, and reshaping when heated to above 200 °C (Supporting Information, Figure S12b,d,e). Interestingly, the coalesced NCs retain the hexagonal high-chalcocite crystal structure even at temperatures as high as 240 °C (Supporting Information, Figure S12e), despite the pronounced increase in size and reshaping. This can be attributed to the high stability of the hexagonal high-chalcocite structure, which is the thermodynamically stable phase of bulk Cu_2S at temperatures above 105 °C.[69−71] Despite the differences in the NC environment between *in situ* heating TEM (vacuum) and hot liquid reaction (excess coordinating ligands in solution), the significant changes in the morphology and size observed by *in situ* heating TEM unambiguously demonstrate the very dynamic nature of nanoscale $Cu_{2-x}S$ at elevated temperatures and can thus be taken as evidence that similar thermally induced coalescence and morphological reconstruction events will take place under the conditions prevalent during the $Cu_{2-x}S$/ZnS HNC synthesis and will be further modulated by the surfactant ligands and other chemicals present in the reaction medium (*viz.*, TOPO, HDA, zinc oleate, and sulfur) (Supporting Information Figure S13). For example, elemental sulfur dissolved in TOPO (S/TOPO), without additional ligands, yields morphologically indistinct nanoparticles with very large sizes, indicative of uncontrolled aggregation, coalescence, and reconstruction events involving tens of NCs. In contrast, HDA and $Zn(oleate)_2$ hinder the coalescence events, leading to a modest increase in the average diameter (~7 nm, which corresponds to the fusion of ~2 seed

https://dx.doi.org/10.1021/acs.chemmater.0c02817
Chem. Mater. 2021, 33, 102−116

NCs) with shape preservation, while in the presence of TOPO the injected $Cu_{2-x}S$ seed NCs evolve into larger nanodisks (diameter: 10−15 nm, which requires the coalescence of 5−11 seed NCs). As a result, S/TOPO in the presence of additional TOPO and HDA leads to more controlled coalescence events, yielding $Cu_{2-x}S$ nanodisks with diameters ranging from ∼10 to ∼20 nm. The different impacts of HDA and TOPO as ligands can be attributed to their different donor atoms (N and O, respectively) and bulkier nature of the latter, which leads to a weaker but more dynamic and selective binding of TOPO to the facets of $Cu_{2-x}S$ NCs.[45,60,61,72,73] It is worth noting that previous XPS and ^{31}P NMR studies on $Cu_{2-x}S$ NCs prepared by the same method used in the present work revealed that their surface is coated by a layer of dodecanethiolate (DDT) ligands that can be readily exchanged by S^{2-} through a phase transfer procedure to a polar solvent.[73] The outcome of the aggregation and coalescence process will thus be determined by the competition between the native DDT surfactants and the adjuvant ligands in solution for binding sites at the surface of the $Cu_{2-x}S$ seed NCs. Note should be taken that TOPO was used as both a surfactant and solvent for elemental sulfur instead of TOP because the latter has been shown to be an aggressive etchant that induces selective etching and phase transformation of roxbyite $Cu_{1.81}S$ NCs,[74] while binding more strongly to sulfur, thereby decreasing its availability and reactivity.

It should be noted that the binary Cu−S system has a very rich phase diagram, and therefore, $Cu_{2-x}S$ can crystallize in various equilibrium crystal structures,[70,75] for example: (i) monoclinic low-chalcocite Cu_2S, (ii) hexagonal high-chalcocite Cu_2S, (iii) monoclinic djurleite $Cu_{1.94}S$, (iv) cubic digenite $Cu_{1.8}S$, (*v*) triclinic roxbyite $Cu_{1.75-1.86}S$, (vi) orthorhombic anilite $Cu_{1.75}S$, and (vii) hexagonal covellite CuS. In conjunction with the very high solid-state mobility of Cu^+,[58] this makes nanoscale $Cu_{2-x}S$ very susceptible to phase transformations in response to external perturbations such as surfactants (e.g., roxbyite to djurleite in response to etching by TOP or tributylphosphine,[74] digenite to covellite under oxidation and etching in the presence of oleylamine,[76] covellite to high-chalcocite by DDT treatment[77]), strain due to heterointerface formation (either by seeded growth, e.g., djurleite to chalcocite in Cu_2S/PbS,[78] or cation exchange, e.g., roxbyite to djurleite upon Cu^+ for Zn^{2+} cation exchange[41]), oxidation (e.g., djurleite to roxbyite upon phase transfer to water[73]), or size reduction (e.g., low-to high-chalcocite at lower transition temperatures by decreasing the diameter of nanorods[71] or thickness of nanoplatelets[79]). From this perspective, it is noteworthy that the hexagonal high-chalcocite phase of the DDT capped 5.3 nm diameter $Cu_{2-x}S$ seed NCs is maintained in the $Cu_{2-x}S$ segments of the $Cu_{2-x}S$/ZnS HNCs, despite the volume increase and reshaping induced by the aggregation and coalescence events, the changes in the composition of the surfactant layer and the formation of the $Cu_{2-x}S$/ZnS heterointerface. This observation can be rationalized by considering the high thermodynamic stability of the hexagonal high-chalcocite phase of the seed NCs,[41,70,80] which should make phase transformations unfavorable because these are typically thermodynamically driven.

Aggregation and coalescence of colloidal NCs have been reported by many groups, notably in connection with studies of the formation of metal (e.g., Pt, Au, Bi, Pd, etc.[68,81,82]) and semiconductor (e.g., InSb[83]) NCs by aggregative growth. Aggregative growth is the dominant growth mechanism when the monomer formation reaction and NC nucleation are much faster than the overall growth rates, depleting the monomer supply and yielding an ensemble of small NCs which are colloidally unstable because of their large surface/volume ratio and high surface free energies.[68] These primary NCs undergo collisions with their neighbors, aggregating and coalescing when the collisions result in direct NC contact (i.e., when the surface sites happen to be uncoordinated to ligands because of the dynamic nature of the interaction between NCs and surfactant ligands). *In situ* HR-TEM studies have shown that the coalesced NCs immediately undergo structural reconstruction and reshaping into larger and more stable NCs, which provides the driving force for the continuation of the process until either the primary NCs are depleted or their number density drops below a critical threshold that no longer supports a significant collision frequency.[82]

We note that the conditions immediately following the injection of seed NCs into a hot reaction mixture bear similarities with those prevailing in systems dominated by aggregative growth (*viz.*, high temperatures and high concentration of primary NCs, particularly in the injected volume prior to its dispersion in the reaction volume). Therefore, the fate of the injected seed NCs will be determined by a competition between heteroepitaxial growth (which will stabilize the seed NCs), aggregation, and coalescence (which depend on the intrinsic stability of the seed NCs and ligand coverage), and other processes such as Ostwald ripening,[84] cation exchange, and alloying.[85] In case the seed NCs are injected in a medium devoid of monomers, dissolution and/or ripening will prevail at low NC concentrations, while at sufficiently high concentrations, aggregation and coalescence may become the dominant process. It is interesting to note that the injection of a sufficiently high concentration of seed NCs into a hot solvent without NC monomers but with a high concentration of free ligands has been shown to induce ligand-mediated NC coalescence and digestive ripening, yielding NC ensembles with narrow size dispersion.[86]

In the specific case of $Cu_{2-x}S$, MacDonald and co-workers have reported the aggregation and coalescence of nearly spherical (hexagonal bifrustrum) DDT capped low-chalcocite seed NCs into nanorods or nanodisks upon their injection into a hot solution containing specific ligands.[45] $Cu_{2-x}S$ nanorods were selectively formed in the presence of 1,2-hexadecanediol by the oriented attachment of 4 ± 2 NCs along the c-direction of the chalcocite structure, presumably driven by dipolar interactions between the seed NCs because chalcocite Cu_2S NCs likely have a dipole because of the crystal structure anisotropy.[45] In contrast, if oleylamine was used as stabilizing ligand ∼6 seed NCs coalesced laterally into nanodisks,[45] likely because alkylamine binds strongly to the polar facets (i.e., those perpendicular to the *c*-axis) of $Cu_{2-x}S$ NCs, as evidenced by the synthesis of $Cu_{2-x}S$ nanoplatelets.[79] These reports are consistent with the aggregation and coalescence observed in our work (Figure S13, see above), and corroborate that $Cu_{2-x}S$ NCs are very dynamic at temperatures above 200 °C. Considering that the average volume of the $Cu_{2-x}S$ segments of the product $Cu_{2-x}S$/ZnS HNCs corresponds to ∼4 times the volume of the injected $Cu_{2-x}S$ seed NCs, and that most of this volume increase happens in the first 5 s after the injection (see above), we propose that ∼4 $Cu_{2-x}S$ seed NCs undergo a phase of rapid attachment and coalescence through the side (100) or (101) facets prior to the onset of ZnS heteroepitaxial growth (step I, Figure 4). The coalesced NCs subsequently undergo structural reconstruction and reshaping, evolving into larger NCs (mostly nanodisks, but nanorods are also observed), which act as the

https://dx.doi.org/10.1021/acs.chemmater.0c02817
Chem. Mater. 2021, 33, 102−116

effective seeds for the heteroepitaxial growth of ZnS (step II, Figure 4).

It is important to notice that the $Cu_{2-x}S$ seed NCs are injected into a reaction medium in which [ZnS] monomer units are already present because the S-precursor is injected into the hot solution of $Zn(oleate)_2$, 20 s before the seed NCs (Figure 1). A previous work by our group on the synthesis of $CuInS_2$/ZnS HNRs has shown that this allows the ZnS heteronucleation and heteroepitaxial growth rates to outpace competing processes, such as the etching of the $CuInS_2$ seed NCs,[59] Zn^{2+} for Cu^+, or In^{3+} cation exchange, and alloying because of Zn^{2+} interdiffusion.[59,85] In the present case, the ZnS heteroepitaxial growth is clearly not sufficiently fast to outcompete the seed NC aggregation. Nevertheless, the coalescence of the $Cu_{2-x}S$ seed NCs in the presence of [ZnS] monomers is less pronounced than in solutions containing only the ligands and one of the precursors [i.e., $Zn(oleate)_2$ or TOPO/S, see Figure S13]. This suggests that the onset of the ZnS heteroepitaxial growth hampers the aggregation and coalescence process, likely due to a combination of surface stabilization by the binding of the [ZnS] monomer units and reduction of the collision rates.

Intriguingly, the heteroepitaxial overgrowth of wurtzite ZnS (step III, Figure 4) occurs on only one of the (100) facets of the newly formed hexagonal high-chalcocite $Cu_{2-x}S$ seed NCs, resulting in Janus-like $Cu_{2-x}S$/ZnS HNRs (Figure 3, Supporting Information Figures S7 and S10). This differs from the seeded growth of CdSe/CdS core/shell HNRs using wurtzite CdSe NCs,[87,88] in which the anisotropic CdS heteroepitaxial growth occurs on both wurtzite(002) polar facets, albeit with a faster growth rate on the anion-terminated facet, leading to an off-center CdSe core embedded into a CdS rod shell with a diameter slightly larger than that of the core. This asymmetry in the growth rates is even more pronounced in the heteroepitaxial overgrowth of ZnS on wurtzite $CuInS_2$ seed NCs,[59] which occurs almost exclusively on the anion-terminated (002) facet because of the strong ligand coverage of the cation-terminated (002) facet and the side facets, leading to matchstick $CuInS_2$/ZnS core/shell HNRs.

The differences between the seeded growth of wurtzite CdSe/CdS and $CuInS_2$/ZnS HNRs and the Janus-like $Cu_{2-x}S$/ZnS HNRs synthesized in the present work can be rationalized by considering that anisotropic seeded heteroepitaxial growth is a kinetically driven process.[10] Therefore, the facet(s) of the seed NCs that have the highest free energies will lead to the lowest activation energies for heteronucleation and fastest growth rates, outcompeting the other facets for the limited supply of monomers.[10] In the case of wurtzite CdSe and $CuInS_2$ NCs, these facets are the two (002) polar facets, of which the anion-terminated one is the fastest growing both because of its higher free energy and typically lower ligand coverage.[10] In high-chalcocite Cu_2S, the (101) and (100) facets have higher free energy than the (001) facets[79] and will thus be the favored heteronucleation sites. Further, the (100) facets offer 4-fold coordinated sites that facilitate monomer adsorption and incorporation, while the (001) facets are atomically dense with 6-fold coordinated S atoms that kinetically inhibit monomer addition.[79] The faster growth rates of the (100) facets are clearly demonstrated by the tendency of high-chalcocite Cu_2S (and several other $Cu_{2-x}S$ polymorphs) to grow as nanoplatelets and nanodisks under kinetically controlled conditions.[79,89,90]

The heteronucleation of ZnS on the (100) facets of the $Cu_{2-x}S$ seed NCs is further promoted by the small lattice mismatch (*viz.*, 2.1%) between the {100} planes of hexagonal high-chalcocite Cu_2S and hexagonal wurtzite ZnS, which leads to heteroepitaxial growth of ZnS along a direction that is perpendicular to the *c*-axis (step III, Figure 4) [for comparison: the mismatches are 2.8 and 3.9 for $CuInS_2$/ZnS and CdSe/CdS (002) heterointerfaces, respectively].[59,91] This observation also indicates that the heteroepitaxial growth proceeds by the addition of [ZnS] monomer units rather than Zn^{2+} and S^{2-} ions to the (100) facets, so that the facet polarity is preserved throughout the growth, which is consistent with previous reports on other materials.[10,59,92] The selective ZnS heteronucleation on only one of the (100) (or −100) facets of the high-chalcocite $Cu_{2-x}S$ seed NCs can be understood from a kinetics perspective by considering that the heteronucleation rates are much slower than the structural reconstruction and reshaping rates of the newly formed NCs immediately following the aggregation and coalescence events. Given that the (100) and (−100) facets have high free energy, they are likely quickly eliminated because the NC reshaping is driven by the minimization of the surface free energies.[10] This is consistent with the observation that the side facets of $Cu_{2-x}S$ nanodisks and nanoplatelets are not the (100) facets but rather lower index facets such as (111), (120), or (221), which are likely further stabilized by ligands.[89,90] Moreover, the (100) facets of the coalesced $Cu_{2-x}S$ NCs may have different compositions and polarities, analogous to the two Cu-terminated (100) facets and one S-terminated (100) facet reported by Lesyuk et al. for covellite CuS nanoprisms.[93] This would lead to differences in the activation energies for ZnS heteronucleation on different (100) facets further enhancing the kinetic inequalities.

As shown above (Figures 3f and S10), the $Cu_{2-x}S$/ZnS heterointerfaces of the Janus-like $Cu_{2-x}S$/ZnS HNRs synthesized in our work are atomically sharp. This can be attributed to the combination of a small (2.1%) lattice mismatch between the (100) planes of hexagonal high-chalcocite Cu_2S and hexagonal wurtzite ZnS, which results in small heterointerfacial strain fields,[13,14] and lack of Cu^+−Zn^{2+} interdiffusion.[14,41,42] It is interesting to compare the $Cu_{2-x}S$/ZnS heterointerfaces observed in our work, which result from the heteroepitaxial growth of wurtzite ZnS on hexagonal high-chalcocite Cu_2S seed NCs, with those observed by Robinson and co-workers[41] and Schaak and co-workers,[14] which were obtained by the ingrowth of wurtzite ZnS through the topotactic Cu^+ for Zn^{2+} cation exchange in roxbyite $Cu_{1.81}S$ NCs (nearly spherical hexagonal bifrustums with 22 nm diameter and nanorods with 20 nm diameter and 56 nm length, respectively).

In the case of the nearly spherical NCs,[41] "sandwich-like" ZnS/$Cu_{2-x}S$/ZnS HNCs with dual heterointerfaces were obtained. At the early stages of the cation exchange, the central $Cu_{2-x}S$ segment was observed to undergo a solid−solid phase transition to phases with higher thermodynamic stability (djurleite or low-chalcocite) and later return to the roxbyite phase to minimize the heterointerfacial strain energy because the mismatch between the (001) planes of roxbyite and wurtzite ZnS is smaller (1.1%) than those offered by djurleite or low-chalcocite.[41] To relax the interfacial strain atomic steps developed along the $Cu_{2-x}S$/ZnS, dual heterointerfaces of the nearly spherical ZnS/$Cu_{2-x}S$/ZnS HNCs and stacking faults appeared in the copper sulfide central segments.[41] In the case of the $Cu_{1.81}S$ nanorods studied by Schaak and co-workers,[14] three different heteroarchitectures were obtained: single tip ZnS/$Cu_{1.81}S$, dual tip ZnS/$Cu_{1.81}S$/ZnS, and central band $Cu_{1.81}S$/ZnS/$Cu_{1.81}S$ HNRs. In all three heteroarchitectures, the

https://dx.doi.org/10.1021/acs.chemmater.0c02817
Chem. Mater. 2021, 33, 102−116

$Cu_{1.81}S$/ZnS interface consisted of the (100) plane of roxbyite and the (001) plane of wurtzite ZnS because these planes resulted in the smallest lattice mismatch (1.6%), and thus the smallest interfacial strain.[14] Nonetheless, the $Cu_{1.81}S$/ZnS heterointerfaces of the HNRs were observed to exhibit a higher density of defects and more disorder than adjoining regions, leading to higher reactivity, which was exploited to design multicomponent axially segmented HNRs by using multiple successive cation exchange steps.[14]

The differences between the heterointerfaces of the Janus-like $Cu_{2-x}S$/ZnS HNRs synthesized in the present work and those observed in the "sandwich-like" ZnS/$Cu_{1.81}S$/ZnS HNCs and the axially segmented $Cu_{1.81}S$/ZnS HNRs reported, respectively, by Robinson and co-workers[41] and Schaak and co-workers[14] can be attributed to two reasons: (i) smaller interfacial areas in the present case (*viz.*, 30 ± 6 nm^2 in comparison to 380 ± 40 and 310 ± 70 nm^2 for the HNCs reported by Robinson et al.[41] and Schaak et al.,[14] respectively), which facilitate strain accommodation, and (ii) the formation of heterointerfaces by cation exchange and seeded growth occur by fundamentally different processes. In the case of Cu^+ for the Zn^{2+} cation exchange, the wurtzite ZnS phase grows by topoepitaxy at the expense of the $Cu_{1.81}S$ phase, which requires the solid-state diffusion of Zn^{2+} inward and the Cu^+ diffusion outward, while leaving the S^{2-} sublattice essentially unaffected. Given that the activation energies for the Zn^{2+}−Cu^+ interdiffusion are very high (*viz.*, 1.21 eV for Cu^+ in ZnS and 0.54 eV for Zn^{2+} in $Cu_{1.81}S$, in comparison to 0.08 and 0.35 eV for homodiffusion of Cu^+ and Zn^{2+}, respectively[41]), the Cu^+ and Zn^{2+} diffusion fluxes will take place in the plane of the heterointerface itself. Consequently, the $Cu_{2-x}S$/ZnS heterointerface remains extremely dynamic from the onset of the ZnS formation to its end because the reaction front and the heterointerface move together through the template NC. In contrast, in seeded growth, the $Cu_{2-x}S$/ZnS heterointerface is formed at the onset of the ZnS heteroepitaxial growth and is subsequently left undisturbed as the reaction front moves away from it. Therefore, in the absence of interdiffusion and large strain fields (as is the case in the Janus-like $Cu_{2-x}S$/ZnS HNRs synthesized in our work), the $Cu_{2-x}S$/ZnS heterointerface will quickly become the least dynamic and most stable interface in the HNC during the growth process because the tip of the ZnS nanorod segment will be growing by the addition of [ZnS] monomers, while the side facets of both the ZnS and $Cu_{2-x}S$ segments will likely experience ligand-mediated reconstruction and reshaping.

On the other hand, the stacking fault density in the ZnS segments grown by heteroepitaxy seems to be higher than that observed in those grown by cation exchange topoepitaxy. Stacking faults are commonly observed in wurtzite nanorods of II−VI materials grown under kinetic control and have their origin in the small energy difference between the zinc-blende and wurtzite crystal structures of these materials and the inherently dynamic physical-chemical conditions prevalent during fast, kinetically controlled reactions, which lead to fluctuations in the growth rates.[94] In cation exchange topotaxy, the anion sublattice is left essentially undisturbed, while native cations move out and guest cations move in. Therefore, in the absence of large mismatches between parent and product phases, the driving force for the formation of stacking faults is much smaller than during kinetically controlled heteroepitaxial growth. Nevertheless, Robinson et al. observed stacking faults in the copper sulfide segment of the "sandwich-like" ZnS/$Cu_{2-x}S$/ZnS HNCs and in 20% of the fully exchanged ZnS NCs, where they were tentatively attributed to the presence of residual Cu^+.[41] We note that the presence of residual Cu^+ has been reported before in CdS ultrathin nanosheets obtained by topotactic Cu^+ for Cd^{2+} cation exchange in template $Cu_{2-x}S$ nanosheets.[95]

Based on the mechanism discussed above (Figure 4) and the insights gained in our work, design guidelines for the synthesis of Janus-like $Cu_{2-x}S$/ZnS HNRs by seeded growth can be proposed. Increasing the amount of ZnS precursors and reaction temperature (Figure 2) promotes the formation of [ZnS] monomers[59,66] and allows the concentration of [ZnS] monomer units to build up, thus resulting in longer ZnS nanorod segments. High reaction temperatures (e.g., 250 °C) not only accelerate the growth rate of ZnS and reduce the concentration of stacking faults,[66,96] making the product HNRs longer and straighter (Figure 2e−h), but also promote homogeneous nucleation of ZnS NCs and enhance the aggregation and coalescence of the injected $Cu_{2-x}S$ seed NCs. Therefore, the reaction temperature should be kept between 210 and 240 °C. The nature of the ligands and their concentration is a parameter of utmost importance as it modulates the reactivities of both the Zn and S precursors, the aggregation and coalescence of the injected seed NCs, the heteronucleation and heteroepitaxial growth rates, and the reshaping and reconstruction of both the ZnS and the $Cu_{2-x}S$ segments of the product HNCs. Moreover, the outcome of seeded growth reactions is largely dictated by the concentration and characteristics of the seed NCs.[10] The coalescence of the injected $Cu_{2-x}S$ seed NCs thus provides a powerful and versatile way to tailor the product $Cu_{2-x}S$/ZnS HNRs because it is amenable to manipulation by controlling the size, shape, and concentration of the seed NCs, as well as the injection temperature, and the nature and concentration of the ligands present in the reaction medium. As demonstrated by the studies on aggregative growth and digestive ripening discussed above,[68,86] aggregation and coalescence processes can be rationally used to yield NC ensembles with small polydispersity.

$Cu_{2-x}S$/ZnS HNRs as Templates for the Synthesis of $Cu_{2-x}S$ and $CuInS_2$ Nanorods via Cation Exchange. As discussed in the Introduction, cation exchange has been successfully used to obtain Cu-based multinary NCs and multicomponent HNCs.[12−14,18,38−44] From the perspective of rationally designing Cu-based HNRs, the recent work by Schaak and co-workers is particularly relevant, as they introduced design guidelines that enabled the rational synthesis of multicomponent axially segmented HNRs containing up to 8 different segments, yielding 113 different HNRs that were experimentally demonstrated by the authors and synthetically feasible pathways to a total of 65,520 distinct multicomponent metal sulfide HNRs.[14] It is noteworthy that Janus-type $Cu_{2-x}S$/ZnS HNRs similar to those synthesized in the present work are absent in the megalibrary proposed by Schaak and co-workers,[14] despite its staggering diversity. This remarkable absence can be rationalized by considering two inherent constraints of cation exchange reactions: (i) they are often limited by solid-state diffusion fluxes and the interfacial strain between the parent and product phases,[12−14,97] which implies that certain heteroarchitectures may be unattainable, and (ii) in the case of topotactic cation exchange, the size and shape of the product HNCs are imposed by the template NCs, which in the case of the HNRs prepared by Schaak and co-workers were roxbyite $Cu_{1.81}S$ nanorods with 20 nm diameter and 56 nm length. These limitations were circumvented in our work by using a fundamentally different synthesis strategy (heteroepitaxial seeded growth) and small

https://dx.doi.org/10.1021/acs.chemmater.0c02817
Chem. Mater. 2021, 33, 102−116

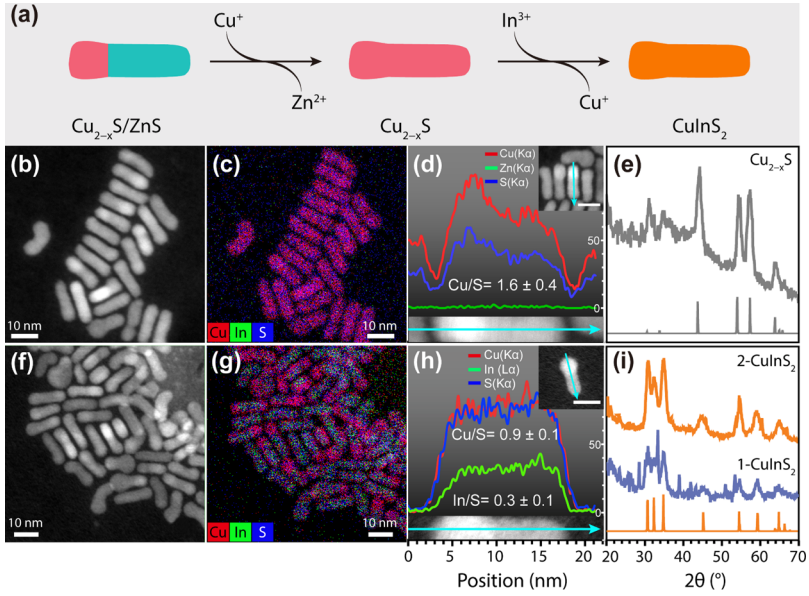

Figure 5. (a) Synthesis scheme of $Cu_{2-x}S$ and $CuInS_2$ nanorods *via* sequential postsynthetic cation exchange in template $Cu_{2-x}S$/ZnS HNRs. (b,c) HAADF-STEM image (b) and corresponding elemental mapping (c) of the product $Cu_{2-x}S$ nanorods. (d) Elemental line scan of a single $Cu_{2-x}S$ nanorod (atomic ratio: Cu/S = 1.6 ± 0.4). The blue arrow in the lower panel indicates the scanned line. Elemental quantification was performed on 100 spots along this line. (e) XRD pattern of the product $Cu_{2-x}S$ nanorods. The grey line indicates the high-chalcocite Cu_2S diffraction pattern (JCPDS card 00-026-1116). (f,g) HAADF-STEM image (f) and corresponding elemental mapping (g) of the product $CuInS_2$ nanorods. (h) Elemental line scan of a single $CuInS_2$ nanorod (atomic ratio: Cu/S = 0.9 ± 0.1; In/S = 0.3 ± 0.1). The blue arrow in the lower panel indicates the scanned line. Elemental quantification was performed on 100 spots along this line. (i) XRD patterns of the nonstoichiometric exchanged (1-$CuInS_2$, In/Cu ∼ 0.3) and stoichiometric exchanged (2-$CuInS_2$, In/Cu ∼ 1.0) product $CuInS_2$ nanorods. The sharp orange line indicates the wurtzite $CuInS_2$ diffraction pattern (JCPDS card 01-077-9459).

seed NCs (5.3 nm high-chalcocite $Cu_{2-x}S$ NCs). We note that the availability of the Janus-type $Cu_{2-x}S$/ZnS HNRs synthesized in our work paves the way to an even larger megalibrary of HNRs because they may be regarded as "second generation synthons" (in the terminology proposed Schaak and co-workers),[13,14] and as such used as starting points for the rational synthesis of higher generations of HNRs using the design guidelines proposed in ref 14 in combination with recent insights on the factors governing the thermodynamics and kinetics of cation exchange reactions.[12−14,18,40,42,97,98] Moreover, their conversion to $Cu_{2-x}S$ nanorods by postsynthetic topotactic Zn^{2+} for the Cu^+ cation exchange offers a way to circumvent the size limitations of the currently available methods, yielding high-chalcocite $Cu_{2-x}S$ nanorods with diameters below 10 nm, which are in turn useful as first generation synthons in both cation exchange and seeded growth synthesis strategies. As a proof of principle and to illustrate the feasibility of these synthesis routes, in this section, we demonstrate the topotactic conversion of Janus-type $Cu_{2-x}S$/ZnS HNRs into $Cu_{2-x}S$ nanorods, which are subsequently used as templates for the synthesis of $CuInS_2$ nanorods by partial Cu^+ for In^{3+} exchange.

Figure 5a schematically depicts the pathway for synthesizing $Cu_{2-x}S$ and $CuInS_2$ nanorods by the postsynthetic cation exchange using the $Cu_{2-x}S$/ZnS HNRs synthesized in this work as templates. The $Cu_{2-x}S$ nanorods were obtained by full Zn^{2+} for Cu^+ cation exchange (see Experimental Section for details). The HAADF-STEM image of the product NCs shows that the shape and size of the template $Cu_{2-x}S$/ZnS HNCs were preserved after the Zn^{2+} for Cu^+ cation exchange (Figure 5b). Two-dimensional elemental mapping was employed to analyze the composition of the product nanorods. The acquired image shows that the NCs are composed of Cu^+ and S^{2-} only (Figure 5c). The elemental line scan of a single $Cu_{2-x}S$ nanorod reveals the composition distribution of each element (Figure 5d). It is found that the nanorod is made up of Cu and S ions with a molar ratio of Cu/S = 1.6 ± 0.4. Moreover, it should be noted that a difference in contrast is still observed in the HAADF-STEM image of a single $Cu_{2-x}S$ nanorod (inset in Figure 5d). Considering that this contrast is not because of compositional differences because the Cu/S ratio throughout the nanorod is essentially the same (Figure 5d), we conclude that the product nanorods are probably "match-like" rods with a thicker head, which is consistent with the 3d tomography results discussed above (Figure 3g) and with HRTEM images of the product $Cu_{2-x}S$ nanorods (Supporting Information, Figure S14). FT patterns of single $Cu_{2-x}S$ nanorods at both the thicker and thinner parts are similar and can be indexed to hexagonal high-chalcocite Cu_2S viewed along the [001] direction (Supporting Information, Figure S14). The XRD pattern of an ensemble of $Cu_{2-x}S$ nanorods was also measured and can be indexed to hexagonal high-chalcocite Cu_2S (2θ = 43.8, 53.7, and 57°) (Figure 5e), without the characteristic peaks of wurtzite ZnS (2θ = 31.4, 33.3, and 35.7°). This confirms that the ZnS segments of the $Cu_{2-x}S$/ZnS HNRs were successfully converted to $Cu_{2-x}S$ by topotactic Zn^{2+} for the Cu^+ exchange.

The conversion of the product $Cu_{2-x}S$ nanorods into $CuInS_2$ nanorods was achieved by partial Cu^+ for In^{3+} cation exchange (see Experimental Section for details). The product $CuInS_2$ nanorods inherit the size, polydispersity, and shape of the template $Cu_{2-x}S$ nanorods (Figure 5f). Two-dimensional elemental mapping shows that the product nanorods contain Cu^+, S^{2-}, and In^{3+}, indicating the successful incorporation of indium (Figure 5g,h). However, short reaction times lead to substoichiometric nanorods (e.g., In/S = 0.3 ± 0.1; Cu/S = 0.9 ± 0.1, in a single nanorod, Figure 5h) displaying inhomogeneous In^{3+} distributions (Figure 5g). To obtain nearly stoichiometric

https://dx.doi.org/10.1021/acs.chemmater.0c02817
Chem. Mater. 2021, 33, 102−116

$CuInS_2$ nanorods longer reaction times (overnight) are needed, while keeping all other conditions unchanged. Two-dimensional elemental mapping shows that after overnight reaction, Cu^+, In^{3+}, and S^{2-} are homogeneously distributed and the Cu/In ratio is nearly stoichiometric (Cu/In = 1.1 ± 0.2) (Supporting Information, Figure S15). HRTEM images (Supporting Information, Figure S14d) and XRD pattern (Figure 5i) of the products show that the $CuInS_2$ nanorods have the hexagonal wurtzite crystal structure, demonstrating that the cation exchange is topotactic because the hexagonal sulfide sublattice of the template high-chalcocite $Cu_{2-x}S$ nanorods is preserved, which is consistent with previous reports.[38,61] The average diameter of the product $CuInS_2$ nanorods (6.8 ± 1.6 nm, Supporting Information Figure S16) is sufficiently small to induce quantum confinement effects because the exciton Bohr radius of $CuInS_2$ is ∼4.1 nm.[18,72,99] Photoluminescence was however not observed, likely due to the large volume of the nanorods and the lack of a surface passivating shell.[72,99] This is consistent with the radiative recombination mechanism proposed for NCs of $CuInS_2$ and related I−III−VI_2 semiconductors, which involves a localized hole and a delocalized conduction band electron, which can be easily trapped at the unpassivated surface states.[99] These electron traps may be eliminated by shell overgrowth of wider band gap semiconductors, such as CdS and ZnS.[61,99,100] This is however beyond the scope of the present work. Furthermore, the absorption spectrum of the $CuInS_2$ nanorods show a weak and broad NIR band (Supporting Information, Figure S17), which can be ascribed to LSPR because of a small excess of free carriers induced by cation vacancies, either Cu-vacancies,[18,67] or In-vacancies.[101] Excess carriers are also known to induce photoluminescence quenching because they enhance non-radiative Auger recombination rates.[99]

CONCLUSIONS

In this work, we have developed a multistep synthetic strategy toward colloidal $Cu_{2-x}S$/ZnS Janus-type HNRs and $Cu_{2-x}S$ and $CuInS_2$ nanorods with diameters in the quantum confinement regime (*viz.*, 6−7 nm, exciton Bohr radii for $Cu_{2-x}S$ and $CuInS_2$ are ∼5 and 4.1 nm, respectively).[18,49,99] The Janus-type $Cu_{2-x}S$/ZnS HNRs are obtained by the injection of hexagonal high-chalcocite $Cu_{2-x}S$ seed NCs in a hot zinc oleate solution in the presence of suitable surfactants, 20 s after the injection of sulfur precursors (S/TOPO). We found that in the first few seconds after the injection, the $Cu_{2-x}S$ seed NCs undergo rapid aggregation and coalescence, forming larger NCs that act as the effective seeds for heteronucleation and growth of ZnS from the [ZnS] monomers present in the reaction medium. The ZnS heteronucleation occurs on a single (100) facet of the $Cu_{2-x}S$ seed NCs and is followed by fast anisotropic growth of ZnS along a direction that is perpendicular to the *c*-axis, thus leading to $Cu_{2-x}S$/ZnS Janus-type HNRs. Structural analyses demonstrate that the hexagonal high-chalcocite crystal structure of the injected $Cu_{2-x}S$ seed NCs is preserved in the $Cu_{2-x}S$ segments of the HNRs, attesting the high-thermodynamic stability of this $Cu_{2-x}S$ phase under the conditions prevalent in our experiments. The $Cu_{2-x}S$/ZnS HNRs are subsequently used as templates for the synthesis of $Cu_{2-x}S$ nanorods by topotactic Zn^{2+} for Cu^+ cation exchange. This offers a new synthetic strategy to $Cu_{2-x}S$ nanorods with diameters in a range that is not accessible by direct synthesis (i.e., <10 nm), and without the need of using Cd-chalcogenide-based nanorods as cation exchange templates. The versatility of our synthetic approach is further illustrated by the conversion of the product $Cu_{2-x}S$ nanorods into $CuInS_2$ nanorods by topotactic partial Cu^+ for In^{3+} cation exchange. It is worth noting that Janus-like $Cu_{2-x}S$/ZnS HNRs with diameters in the quantum confinement regime have not yet been obtained, either by direct synthesis or cation exchange-based approaches. Moreover, they are of interest not only as cation exchange templates for single-component $Cu_{2-x}S$ nanorods but also as second-generation synthons in sequential cation exchange synthesis protocols to multicomponent heterostructured nanorods, such as those recently proposed by Schaak and coworkers.[13,14] Our work thus expands the possibilities for the rational synthesis of colloidal multicomponent HNRs by allowing the design principles of postsynthetic heteroepitaxial seeded growth[10] and nanoscale cation exchange[12−14,18,38−42,44,101] to be combined, yielding access to a plethora of multicomponent HNRs with diameters in the quantum confinement regime, in which different functionalities can be integrated in a synergistic way, paving the way to unprecedented nanomaterials with promising properties for a multitude of applications (e.g., photocatalysis, photovoltaics, and nonlinear optics).

ASSOCIATED CONTENT

Supporting Information

The Supporting Information is available free of charge at https://pubs.acs.org/doi/10.1021/acs.chemmater.0c02817.

Detailed description of the procedure used to determine the $Cu_{2-x}S$ NCs concentration; XRD analysis and additional TEM images of $Cu_{2-x}S$/ZnS HNCs synthesized by seeded mediated growth; absorption spectrum of $Cu_{2-x}S$/ZnS HNCs; several more HRTEM images of $Cu_{2-x}S$/ZnS HNCs and corresponding structural analysis; *in situ* heating HAADF-STEM image of $Cu_{2-x}S$ NCs; HRTEM image of $Cu_{2-x}S$ and $CuInS_2$ nanorods; elemental mapping of $CuInS_2$ nanorods; and size distribution histogram of $CuInS_2$ nanorods (PDF)

Animated version of the 3D tomographic reconstruction (MPG)

AUTHOR INFORMATION

Corresponding Author

Celso de Mello Donega − *Debye Institute for Nanomaterials Science, Utrecht University, 3508 TA Utrecht, The Netherlands;* orcid.org/0000-0002-4403-3627; Email: c.demello-donega@uu.nl

Authors

Chenghui Xia − *Debye Institute for Nanomaterials Science, Utrecht University, 3508 TA Utrecht, The Netherlands;* orcid.org/0000-0001-5087-8805

Adrian Pedrazo-Tardajos − *EMAT-University of Antwerp, B-2020 Antwerp, Belgium*

Da Wang − *EMAT-University of Antwerp, B-2020 Antwerp, Belgium*

Johannes D. Meeldijk − *Debye Institute for Nanomaterials Science, Utrecht University, 3508 TA Utrecht, The Netherlands*

Hans C. Gerritsen − *Debye Institute for Nanomaterials Science, Utrecht University, 3508 TA Utrecht, The Netherlands*

Sara Bals − *EMAT-University of Antwerp, B-2020 Antwerp, Belgium*

Complete contact information is available at:

https://dx.doi.org/10.1021/acs.chemmater.0c02817
Chem. Mater. 2021, 33, 102−116

https://pubs.acs.org/10.1021/acs.chemmater.0c02817

Notes

The authors declare no competing financial interest.

■ ACKNOWLEDGMENTS

C.X. acknowledges China Scholarship Council (CSC) for the financial support (grant number 201406330055). C.d.M.D. acknowledges funding from the European Commission for access to the EMAT facilities (grant number EUSMI E180900184). D.W. acknowledges an Individual Fellowship funded by the Marie Sklodowska-Curie Actions (MSCA) in Horizon 2020 program (grant 894254 SuprAtom). S.B. acknowledges support by means of the ERC Consolidator grant no. 815128 REALNANO. The authors thank Donglong Fu for XRD measurements.

■ REFERENCES

(1) Pietryga, J. M.; Park, Y.-S.; Lim, J.; Fidler, A. F.; Bae, W. K.; Brovelli, S.; Klimov, V. I. Spectroscopic and Device Aspects of Nanocrystal Quantum Dots. *Chem. Rev.* **2016**, *116*, 10513−10622.
(2) Panfil, Y. E.; Oded, M.; Banin, U. Colloidal Quantum Nanostructures: Emerging Materials for Display Applications. *Angew. Chem., Int. Ed.* **2018**, *57*, 4274−4295.
(3) Bradshaw, L. R.; Knowles, K. E.; McDowall, S.; Gamelin, D. R. Nanocrystals for Luminescent Solar Concentrators. *Nano Lett.* **2015**, *15*, 1315−1323.
(4) Kagan, C. R.; Lifshitz, E.; Sargent, E. H.; Talapin, D. V. Building Devices from Colloidal Quantum Dots. *Science* **2016**, *353*, aac5523.
(5) Yuan, Y.-P.; Ruan, L.-W.; Barber, J.; Joachim Loo, S. C.; Xue, C. Hetero-Nanostructured Suspended Photocatalysts for Solar-to-Fuel Conversion. *Energy Environ. Sci.* **2014**, *7*, 3934−3951.
(6) Wu, K.; Lian, T. Quantum Confined Colloidal Nanorod Heterostructures for Solar-to-Fuel Conversion. *Chem. Soc. Rev.* **2016**, *45*, 3781−3810.
(7) Palui, G.; Aldeek, F.; Wang, W.; Mattoussi, H. Strategies for Interfacing Inorganic Nanocrystals with Biological Systems Based on Polymer-Coating. *Chem. Soc. Rev.* **2015**, *44*, 193−227.
(8) Pelaz, B.; Alexiou, C.; Alvarez-Puebla, R. A.; Alves, F.; Andrews, A. M.; Ashraf, S.; Balogh, L. P.; Ballerini, L.; Bestetti, A.; Brendel, C.; et al. Diverse Applications of Nanomedicine. *ACS Nano* **2017**, *11*, 2313−2381.
(9) McHugh, K. J.; Jing, L.; Behrens, A. M.; Jayawardena, S.; Tang, W.; Gao, M.; Langer, R.; Jaklenec, A. Biocompatible Semiconductor Quantum Dots as Cancer Imaging Agents. *Adv. Mater.* **2018**, *30*, 1706356.
(10) Donegá, C. d. M. Synthesis and Properties of Colloidal Heteronanocrystals. *Chem. Soc. Rev.* **2011**, *40*, 1512−1546.
(11) Buck, M. R.; Schaak, R. E. Emerging Strategies for the Total Synthesis of Inorganic Nanostructures. *Angew. Chem., Int. Ed.* **2013**, *52*, 6154−6178.
(12) De Trizio, L.; Manna, L. Forging Colloidal Nanostructures via Cation Exchange Reactions. *Chem. Rev.* **2016**, *116*, 10852−10887.
(13) Fenton, J. L.; Steimle, B. C.; Schaak, R. E. Tunable Intraparticle Frameworks for Creating Complex Heterostructured Nanoparticle Libraries. *Science* **2018**, *360*, 513−517.
(14) Steimle, B. C.; Fenton, J. L.; Schaak, R. E. Rational Construction of a Scalable Heterostructured Nanorod Megalibrary. *Science* **2020**, *367*, 418−424.
(15) Rühle, S.; Shalom, M.; Zaban, A. Quantum-Dot-Sensitized Solar Cells. *ChemPhysChem* **2010**, *11*, 2290−2304.
(16) Stolle, C. J.; Harvey, T. B.; Korgel, B. A. Nanocrystal Photovoltaics: A Review of Recent Progress. *Curr. Opin. Chem. Eng.* **2013**, *2*, 160−167.
(17) Klimov, V. I.; Ivanov, S. A.; Nanda, J.; Achermann, M.; Bezel, I.; McGuire, J. A.; Piryatinski, A. Single-Exciton Optical Gain in Semiconductor Nanocrystals. *Nature* **2007**, *447*, 441−446.
(18) van der Stam, W.; Berends, A. C.; de Mello Donegá, C. Prospects of Colloidal Copper Chalcogenide Nanocrystals. *ChemPhysChem* **2016**, *17*, 559−581.
(19) Coughlan, C.; Ibáñez, M.; Dobrozhan, O.; Singh, A.; Cabot, A.; Ryan, K. M. Compound Copper Chalcogenide Nanocrystals. *Chem. Rev.* **2017**, *117*, 5865−6109.
(20) Han, W.; Yi, L.; Zhao, N.; Tang, A.; Gao, M.; Tang, Z. Synthesis and Shape-Tailoring of Copper Sulfide/Indium Sulfide-Based Nanocrystals. *J. Am. Chem. Soc.* **2008**, *130*, 13152−13161.
(21) Roy, P.; Srivastava, S. K. Nanostructured Copper Sulfides: Synthesis, Properties and Applications. *CrystEngComm* **2015**, *17*, 7801−7815.
(22) Sun, S.; Li, P.; Liang, S.; Yang, Z. Diversified Copper Sulfide ($Cu_{2-x}S$) Micro-/Nanostructures: A Comprehensive Review on Synthesis, Modifications and Applications. *Nanoscale* **2017**, *9*, 11357−11404.
(23) Zhang, J.; Yu, J.; Zhang, Y.; Li, Q.; Gong, J. R. Visible Light Photocatalytic H_2-Production Activity of CuS/ZnS Porous Nanosheets Based on Photoinduced Interfacial Charge Transfer. *Nano Lett.* **2011**, *11*, 4774−4779.
(24) Ben-Shahar, Y.; Banin, U. Hybrid Semiconductor−Metal Nanorods as Photocatalysts. *Top. Curr. Chem.* **2016**, *374*, 54.
(25) Kamat, P. V. Manipulation of Charge Transfer Across Semiconductor Interface. A Criterion That Cannot Be Ignored in Photocatalyst Design. *J. Phys. Chem. Lett.* **2012**, *3*, 663−672.
(26) Wu, K.; Zhu, H.; Lian, T. Ultrafast Exciton Dynamics and Light-Driven H_2 Evolution in Colloidal Semiconductor Nanorods and Pt-Tipped Nanorods. *Acc. Chem. Res.* **2015**, *48*, 851−859.
(27) Manzi, A.; Simon, T.; Sonnleitner, C.; Döblinger, M.; Wyrwich, R.; Stern, O.; Stolarczyk, J. K.; Feldmann, J. Light-Induced Cation Exchange for Copper Sulfide Based CO_2 Reduction. *J. Am. Chem. Soc.* **2015**, *137*, 14007−14010.
(28) Rivest, J. B.; Swisher, S. L.; Fong, L.-K.; Zheng, H.; Alivisatos, A. P. Assembled Monolayer Nanorod Heterojunctions. *ACS Nano* **2011**, *5*, 3811−3816.
(29) Dorfs, D.; Salant, A.; Popov, I.; Banin, U. ZnSe Quantum Dots Within CdS Nanorods: A Seeded-Growth Type-II System. *Small* **2008**, *4*, 1319−1323.
(30) Kirsanova, M.; Nemchinov, A.; Hewa-Kasakarage, N. N.; Schmall, N.; Zamkov, M. Synthesis of ZnSe/CdS/ZnSe Nanobarbells Showing Photoinduced Charge Separation. *Chem. Mater.* **2009**, *21*, 4305−4309.
(31) Oh, N.; Kim, B. H.; Cho, S.-Y.; Nam, S.; Rogers, S. P.; Jiang, Y.; Flanagan, J. C.; Zhai, Y.; Kim, J.-H.; Lee, J.; et al. Double-Heterojunction Nanorod Light-Responsive LEDs for Display Applications. *Science* **2017**, *355*, 616−619.
(32) Connor, S. T.; Hsu, C.-M.; Weil, B. D.; Aloni, S.; Cui, Y. Phase Transformation of Biphasic Cu_2S−$CuInS_2$ to Monophasic $CuInS_2$ Nanorods. *J. Am. Chem. Soc.* **2009**, *131*, 4962−4966.
(33) Kruszynska, M.; Borchert, H.; Parisi, J.; Kolny-Olesiak, J. Synthesis and Shape Control of $CuInS_2$ Nanoparticles. *J. Am. Chem. Soc.* **2010**, *132*, 15976−15986.
(34) Chang, J.-Y.; Cheng, C.-Y. Facile One-Pot Synthesis of Copper Sulfide−Metal Chalcogenide Anisotropic Heteronanostructures in a Noncoordinating Solvent. *Chem. Commun.* **2011**, *47*, 9089−9091.
(35) Kolny-Olesiak, J. Synthesis of Copper Sulphide-Based Hybrid Nanostructures and Their Application in Shape Control of Colloidal Semiconductor Nanocrystals. *CrystEngComm* **2014**, *16*, 9381−9390.
(36) Han, S.-K.; Gong, M.; Yao, H.-B.; Wang, Z.-M.; Yu, S.-H. One-Pot Controlled Synthesis of Hexagonal-Prismatic $Cu_{1.94}S$-ZnS, $Cu_{1.94}S$-ZnS-$Cu_{1.94}S$, and $Cu_{1.94}S$-ZnS-$Cu_{1.94}S$-ZnS-$Cu_{1.94}S$ Heteronanostructures. *Angew. Chem., Int. Ed.* **2012**, *51*, 6365−6368.
(37) Zhai, Y.; Shim, M. Cu_2S/ZnS Heterostructured Nanorods: Cation Exchange vs. Solution−Liquid−Solid-like Growth. *ChemPhysChem* **2016**, *17*, 741−751.
(38) van der Stam, W.; Berends, A. C.; Rabouw, F. T.; Willhammar, T.; Ke, X.; Meeldijk, J. D.; Bals, S.; de Mello Donegá, C. Luminescent $CuInS_2$ Quantum Dots by Partial Cation Exchange in $Cu_{2-x}S$ Nanocrystals. *Chem. Mater.* **2015**, *27*, 621−628.

(39) Liu, Y.; Yin, D.; Swihart, M. T. Valence Selectivity of Cation Incorporation into Covellite CuS Nanoplatelets. *Chem. Mater.* **2018**, *30*, 1399−1407.
(40) Hinterding, S. O. M.; Berends, A. C.; Kurttepeli, M.; Moret, M.-E.; Meeldijk, J. D.; Bals, S.; van der Stam, W.; de Mello Donega, C. Tailoring Cu^{+} for Ga^{3+} Cation Exchange in $Cu_{2-x}S$ and $CuInS_2$ Nanocrystals by Controlling the Ga Precursor Chemistry. *ACS Nano* **2019**, *13*, 12880−12893.
(41) Ha, D.-H.; Caldwell, A. H.; Ward, M. J.; Honrao, S.; Mathew, K.; Hovden, R.; Koker, M. K. A.; Muller, D. A.; Hennig, R. G.; Robinson, R. D. Solid−Solid Phase Transformations Induced through Cation Exchange and Strain in 2D Heterostructured Copper Sulfide Nanocrystals. *Nano Lett.* **2014**, *14*, 7090−7099.
(42) Liu, Y.; Liu, M.; Yin, D.; Qiao, L.; Fu, Z.; Swihart, M. T. Selective Cation Incorporation into Copper Sulfide Based Nanoheterostructures. *ACS Nano* **2018**, *12*, 7803−7811.
(43) Adel, P.; Wolf, A.; Kodanek, T.; Dorfs, D. Segmented CdSe@CdS/ZnS Nanorods Synthesized via a Partial Ion Exchange Sequence. *Chem. Mater.* **2014**, *26*, 3121−3127.
(44) van der Stam, W.; Bladt, E.; Rabouw, F. T.; Bals, S.; de Mello Donega, C. Near-Infrared Emitting $CuInSe_2/CuInS_2$ Dot Core/Rod Shell Heteronanorods by Sequential Cation Exchange. *ACS Nano* **2015**, *9*, 11430−11438.
(45) Robinson, E. H.; Turo, M. J.; Macdonald, J. E. Controlled Surface Chemistry for the Directed Attachment of Copper(I) Sulfide Nanocrystals. *Chem. Mater.* **2017**, *29*, 3854−3857.
(46) Kruszynska, M.; Borchert, H.; Bachmatiuk, A.; Rümmeli, M. H.; Büchner, B.; Parisi, J.; Kolny-Olesiak, J. Size and Shape Control of Colloidal Copper(I) Sulfide Nanorods. *ACS Nano* **2012**, *6*, 5889−5896.
(47) Al-Shakban, M.; Matthews, P. D.; Deogratias, G.; McNaughter, P. D.; Raftery, J.; Vitorica-Yrezabal, I.; Mubofu, E. B.; O'Brien, P. Novel Xanthate Complexes for the Size-Controlled Synthesis of Copper Sulfide Nanorods. *Inorg. Chem.* **2017**, *56*, 9247−9254.
(48) Zhai, Y.; Shim, M. Effects of Copper Precursor Reactivity on the Shape and Phase of Copper Sulfide Nanocrystals. *Chem. Mater.* **2017**, *29*, 2390−2397.
(49) Zhao, Y.; Pan, H.; Lou, Y.; Qiu, X.; Zhu, J.; Burda, C. Plasmonic $Cu_{2-x}S$ Nanocrystals: Optical and Structural Properties of Copper-Deficient Copper(I) Sulfides. *J. Am. Chem. Soc.* **2009**, *131*, 4253−4261.
(50) Sadtler, B.; Demchenko, D. O.; Zheng, H.; Hughes, S. M.; Merkle, M. G.; Dahmen, U.; Wang, L.-W.; Alivisatos, A. P. Selective Facet Reactivity during Cation Exchange in Cadmium Sulfide Nanorods. *J. Am. Chem. Soc.* **2009**, *131*, 5285−5293.
(51) Yi, L.; Tang, A.; Niu, M.; Han, W.; Hou, Y.; Gao, M. Synthesis and Self-Assembly of $Cu_{1.94}S$-ZnS Heterostructured Nanorods. *CrystEngComm* **2010**, *12*, 4124−4130.
(52) Huang, F.; Wang, X.; Xu, J.; Chen, D.; Wang, Y. A Plasmonic Nano-Antenna with Controllable Resonance Frequency: $Cu_{1.94}S$-ZnS Dimeric Nanoheterostructure Synthesized in Solution. *J. Mater. Chem.* **2012**, *22*, 22614−22618.
(53) Ye, H.; Tang, A.; Huang, L.; Wang, Y.; Yang, C.; Hou, Y.; Peng, H.; Zhang, F.; Teng, F. Facile One-Step Synthesis and Transformation of Cu(I)-Doped Zinc Sulfide Nanocrystals to $Cu_{1.94}S$−ZnS Heterostructured Nanocrystals. *Langmuir* **2013**, *29*, 8728−8735.
(54) Yi, L.; Liu, Y.; Yang, N.; Tang, Z.; Zhao, H.; Ma, G.; Su, Z.; Wang, D. One Dimensional $CuInS_2$−ZnS Heterostructured Nanomaterials as Low-Cost and High-Performance Counter Electrodes of Dye-Sensitized Solar Cells. *Energy Environ. Sci.* **2013**, *6*, 835−840.
(55) Li, J.; Bloemen, M.; Parisi, J.; Kolny-Olesiak, J. Role of Copper Sulfide Seeds in the Growth Process of $CuInS_2$ Nanorods and Networks. *ACS Appl. Mater. Interfaces* **2014**, *6*, 20535−20543.
(56) Chen, Y.; Zhao, S.; Wang, X.; Peng, Q.; Lin, R.; Wang, Y.; Shen, R.; Cao, X.; Zhang, L.; Zhou, G.; et al. Synergetic Integration of $Cu_{1.94}S$−$Zn_xCd_{1-x}S$ Heteronanorods for Enhanced Visible-Light-Driven Photocatalytic Hydrogen Production. *J. Am. Chem. Soc.* **2016**, *138*, 4286−4289.
(57) Yu, Z.; Chen, Z.; Chen, Y.; Peng, Q.; Lin, R.; Wang, Y.; Shen, R.; Cao, X.; Zhuang, Z.; Li, Y. Photocatalytic Hydrogenation of Nitroarenes using $Cu_{1.94}S$-$Zn_{0.23}Cd_{0.77}S$ Heteronanorods. *Nano Res.* **2018**, *11*, 3730−3738.
(58) Wang, L.-W. High Chalcocite Cu_2S: A Solid-Liquid Hybrid Phase. *Phys. Rev. Lett.* **2012**, *108*, 085703.
(59) Xia, C.; Winckelmans, N.; Prins, P. T.; Bals, S.; Gerritsen, H. C.; de Mello Donegá, C. Near-Infrared-Emitting $CuInS_2$/ZnS Dot-in-Rod Colloidal Heteronanorods by Seeded Growth. *J. Am. Chem. Soc.* **2018**, *140*, 5755−5763.
(60) Wang, Y.; Hu, Y.; Zhang, Q.; Ge, J.; Lu, Z.; Hou, Y.; Yin, Y. One-Pot Synthesis and Optical Property of Copper(I) Sulfide Nanodisks. *Inorg. Chem.* **2010**, *49*, 6601−6608.
(61) Xia, C.; Meeldijk, J. D.; Gerritsen, H. C.; de Mello Donegá, C. Highly Luminescent Water-Dispersible NIR-Emitting Wurtzite $CuInS_2$/ZnS Core/Shell Colloidal Quantum Dots. *Chem. Mater.* **2017**, *29*, 4940−4951.
(62) Klinger, M.; Jäger, A. Crystallographic Tool Box (CrysTBox): Automated Tools for Transmission Electron Microscopists and Crystallographers. *J. Appl. Crystallogr.* **2015**, *48*, 2012−2018.
(63) Klinger, M. CrysTBox − Crystallographic Toolbox; Institute of Physics of the Czech Academy of Sciences, 2015, https://www.fzu.cz/~klinger/crystbox.pdf (accessed Oct 26, 2020).
(64) Altantzis, T.; Lobato, I.; De Backer, A.; Béché, A.; Zhang, Y.; Basak, S.; Porcu, M.; Xu, Q.; Sánchez-Iglesias, A.; Liz-Marzán, L. M.; et al. Three-Dimensional Quantification of the Facet Evolution of Pt Nanoparticles in a Variable Gaseous Environment. *Nano Lett.* **2019**, *19*, 477−481.
(65) Kim, D.; Lee, Y. K.; Lee, D.; Kim, W. D.; Bae, W. K.; Lee, D. C. Colloidal Dual-Diameter and Core-Position-Controlled Core/Shell Cadmium Chalcogenide Nanorods. *ACS Nano* **2017**, *11*, 12461−12472.
(66) Li, L. S.; Pradhan, N.; Wang, Y.; Peng, X. High Quality ZnSe and ZnS Nanocrystals Formed by Activating Zinc Carboxylate Precursors. *Nano Lett.* **2004**, *4*, 2261−2264.
(67) Bryks, W.; Lupi, E.; Ngo, C.; Tao, A. R. Digenite Nanosheets Synthesized by Thermolysis of Layered Copper-Alkanethiolate Frameworks. *J. Am. Chem. Soc.* **2016**, *138*, 13717−13725.
(68) Wang, F.; Richards, V. N.; Shields, S. P.; Buhro, W. E. Kinetics and Mechanisms of Aggregative Nanocrystal Growth. *Chem. Mater.* **2014**, *26*, 5−21.
(69) Buerger, M. J.; Wuensch, B. J. Distribution of Atoms in High Chalcocite, Cu_2S. *Science* **1963**, *141*, 276−277.
(70) Chakrabarti, D. J.; Laughlin, D. E. The Cu-S (Copper-Sulfur) System. *Bull. Alloy Phase Diagrams* **1983**, *4*, 254−271.
(71) Rivest, J. B.; Fong, L.-K.; Jain, P. K.; Toney, M. F.; Alivisatos, A. P. Size Dependence of a Temperature-Induced Solid−Solid Phase Transition in Copper(I) Sulfide. *J. Phys. Chem. Lett.* **2011**, *2*, 2402−2406.
(72) Xia, C.; Wu, W.; Yu, T.; Xie, X.; van Oversteeg, C.; Gerritsen, H. C.; de Mello Donega, C. Size-Dependent Band-Gap and Molar Absorption Coefficients of Colloidal $CuInS_2$ Quantum Dots. *ACS Nano* **2018**, *12*, 8350−8361.
(73) van Oversteeg, C. H. M.; Oropeza, F. E.; Hofmann, J. P.; Hensen, E. J. M.; de Jongh, P. E.; de Mello Donega, C. Water-Dispersible Copper Sulfide Nanocrystals via Ligand Exchange of 1-Dodecanethiol. *Chem. Mater.* **2019**, *31*, 541−552.
(74) Nelson, A.; Ha, D.-H.; Robinson, R. D. Selective Etching of Copper Sulfide Nanoparticles and Heterostructures through Sulfur Abstraction: Phase Transformations and Optical Properties. *Chem. Mater.* **2016**, *28*, 8530−8541.
(75) Mumme, W. G.; Sparrow, G. J.; Walker, G. S. Roxbyite, a New Copper Sulphide Mineral from the Olympic Dam Deposit, Roxby Downs, South Australia. *Mineral. Mag.* **1988**, *52*, 323−330.
(76) Liu, L.; Zhong, H.; Bai, Z.; Zhang, T.; Fu, W.; Shi, L.; Xie, H.; Deng, L.; Zou, B. Controllable Transformation from Rhombohedral $Cu_{1.8}S$ Nanocrystals to Hexagonal CuS Clusters: Phase- and Composition-Dependent Plasmonic Properties. *Chem. Mater.* **2013**, *25*, 4828−4834.

https://dx.doi.org/10.1021/acs.chemmater.0c02817
Chem. Mater. 2021, 33, 102−116

(77) Liu, Y.; Liu, M.; Swihart, M. T. Reversible Crystal Phase Interconversion between Covellite CuS and High Chalcocite Cu_2S Nanocrystals. *Chem. Mater.* **2017**, *29*, 4783−4791.
(78) Zhuang, T.-T.; Fan, F.-J.; Gong, M.; Yu, S.-H. $Cu_{1.94}S$ Nanocrystal Seed Mediated Solution-Phase Growth of Unique Cu_2S−PbS Heteronanostructures. *Chem. Commun.* **2012**, *48*, 9762−9764.
(79) Sigman, M. B.; Ghezelbash, A.; Hanrath, T.; Saunders, A. E.; Lee, F.; Korgel, B. A. Solventless Synthesis of Monodisperse Cu_2S Nanorods, Nanodisks, and Nanoplatelets. *J. Am. Chem. Soc.* **2003**, *125*, 16050−16057.
(80) Liu, L.; Liu, C.; Fu, W.; Deng, L.; Zhong, H. Phase Transformations of Copper Sulfide Nanocrystals: Towards Highly Efficient Quantum-Dot-Sensitized Solar Cells. *ChemPhysChem* **2016**, *17*, 771−776.
(81) Polte, J.; Erler, R.; Thünemann, A. F.; Sokolov, S.; Ahner, T. T.; Rademann, K.; Emmerling, F.; Kraehnert, R. Nucleation and Growth of Gold Nanoparticles Studied via in situ Small Angle X-ray Scattering at Millisecond Time Resolution. *ACS Nano* **2010**, *4*, 1076−1082.
(82) Yuk, J. M.; Park, J.; Ercius, P.; Kim, K.; Hellebusch, D. J.; Crommie, M. F.; Lee, J. Y.; Zettl, A.; Alivisatos, A. P. High-Resolution EM of Colloidal Nanocrystal Growth Using Graphene Liquid Cells. *Science* **2012**, *336*, 61−64.
(83) Busatto, S.; Ruiter, M. d.; Jastrzebski, J. T. B. H.; Albrecht, W.; Pinchetti, V.; Brovelli, S.; Bals, S.; Moret, M.-E.; de Mello Donega, C. Luminescent Colloidal InSb Quantum Dots from In Situ Generated Single-Source Precursor. *ACS Nano* **2020**, *14*, 13146−13160.
(84) Yang, H.; Hamachi, L. S.; Rreza, I.; Wang, W.; Chan, E. M. Design Rules for One-Step Seeded Growth of Nanocrystals: Threading the Needle between Secondary Nucleation and Ripening. *Chem. Mater.* **2019**, *31*, 4173−4183.
(85) Berends, A. C.; van der Stam, W.; Hofmann, J. P.; Bladt, E.; Meeldijk, J. D.; Bals, S.; de Mello Donega, C. Interplay between Surface Chemistry, Precursor Reactivity, and Temperature Determines Outcome of ZnS Shelling Reactions on $CuInS_2$ Nanocrystals. *Chem. Mater.* **2018**, *30*, 2400−2413.
(86) Razgoniaeva, N.; Yang, M.; Garrett, P.; Kholmicheva, N.; Moroz, P.; Eckard, H.; Royo Romero, L.; Porotnikov, D.; Khon, D.; Zamkov, M. Just Add Ligands: Self-Sustained Size Focusing of Colloidal Semiconductor Nanocrystals. *Chem. Mater.* **2018**, *30*, 1391−1398.
(87) Talapin, D. V.; Nelson, J. H.; Shevchenko, E. V.; Aloni, S.; Sadtler, B.; Alivisatos, A. P. Seeded Growth of Highly Luminescent CdSe/CdS Nanoheterostructures with Rod and Tetrapod Morphologies. *Nano Lett.* **2007**, *7*, 2951−2959.
(88) Carbone, L.; Nobile, C.; De Giorgi, M.; Sala, F. D.; Morello, G.; Pompa, P.; Hytch, M.; Snoeck, E.; Fiore, A.; Franchini, I. R.; Nadasan, M.; Silvestre, A. F.; Chiodo, L.; Kudera, S.; Cingolani, R.; Krahne, R.; Manna, L. Synthesis and Micrometer-Scale Assembly of Colloidal CdSe/CdS Nanorods Prepared by a Seeded Growth Approach. *Nano Lett.* **2007**, *7*, 2942−2950.
(89) Li, W.; Shavel, A.; Guzman, R.; Rubio-Garcia, J.; Flox, C.; Fan, J.; Cadavid, D.; Ibáñez, M.; Arbiol, J.; Morante, J. R.; et al. Morphology evolution of $Cu_{2-x}S$ nanoparticles: from spheres to dodecahedrons. *Chem. Commun.* **2011**, *47*, 10332−10334.
(90) van der Stam, W.; Gradmann, S.; Altantzis, T.; Ke, X.; Baldus, M.; Bals, S.; de Mello Donega, C. Shape Control of Colloidal $Cu_{2-x}S$ Polyhedral Nanocrystals by Tuning the Nucleation Rates. *Chem. Mater.* **2016**, *28*, 6705−6715.
(91) Demortière, A.; Leonard, D. N.; Petkov, V.; Chapman, K.; Chattopadhyay, S.; She, C.; Cullen, D. A.; Shibata, T.; Pelton, M.; Shevchenko, E. V. Strain-Driven Stacking Faults in CdSe/CdS Core/Shell Nanorods. *J. Phys. Chem. Lett.* **2018**, *9*, 1900−1906.
(92) Bladt, E.; Van Dijk-Moes, R. J. A.; Peters, J.; Montanarella, F.; De Mello Donega, C.; Vanmaekelbergh, D.; Bals, S. Atomic Structure of Wurtzite CdSe (Core)/CdS (Giant Shell) Nanobullets Related to Epitaxy and Growth. *J. Am. Chem. Soc.* **2016**, *138*, 14288−14293.
(93) Lesyuk, R.; Klein, E.; Yaremchuk, I.; Klinke, C. Copper Sulfide Nanosheets with Shape-Tunable Plasmonic Properties in the NIR Region. *Nanoscale* **2018**, *10*, 20640−20651.
(94) Hughes, S. M.; Alivisatos, A. P. Anisotropic Formation and Distribution of Stacking Faults in II−VI Semiconductor Nanorods. *Nano Lett.* **2013**, *13*, 106−110.
(95) van der Stam, W.; Akkerman, Q. A.; Ke, X.; van Huis, M. A.; de Mello Donega, C.; de Mello Donega, C. Solution-Processable Ultrathin Size- and Shape-Controlled Colloidal $Cu_{2-x}S$ Nanosheets. *Chem. Mater.* **2015**, *27*, 283−291.
(96) Zhuang, T.-T.; Yu, P.; Fan, F.-J.; Wu, L.; Liu, X.-J.; Yu, S.-H. Controlled Synthesis of Kinked Ultrathin ZnS Nanorods/Nanowires Triggered by Chloride Ions: A Case Study. *Small* **2014**, *10*, 1394−1402.
(97) Groeneveld, E.; Witteman, L.; Lefferts, M.; Ke, X.; Bals, S.; Van Tendeloo, G.; de Mello Donega, C. Tailoring ZnSe−CdSe Colloidal Quantum Dots via Cation Exchange: From Core/Shell to Alloy Nanocrystals. *ACS Nano* **2013**, *7*, 7913−7930.
(98) Mu, L.; Wang, F.; Sadtler, B.; Loomis, R. A.; Buhro, W. E. Influence of the Nanoscale Kirkendall Effect on the Morphology of Copper Indium Disulfide Nanoplatelets Synthesized by Ion Exchange. *ACS Nano* **2015**, *9*, 7419−7428.
(99) Berends, A. C.; Mangnus, M. J. J.; Xia, C.; Rabouw, F. T.; de Mello Donega, C. Optoelectronic Properties of Ternary I−III−VI_2 Semiconductor Nanocrystals: Bright Prospects with Elusive Origins. *J. Phys. Chem. Lett.* **2019**, *10*, 1600−1616.
(100) Xia, C.; Wang, W.; Du, L.; Rabouw, F. T.; van den Heuvel, D. J.; Mattoussi, H.; de Mello Donega, C.; de Mello Donega, C. Förster Resonance Energy Transfer between Colloidal $CuInS_2$/ZnS Quantum Dots and Dark Quenchers. *J. Phys. Chem. C* **2020**, *124*, 1717−1731.
(101) Berends, A. C.; Meeldijk, J. D.; Van Huis, M. A.; de Mello Donega, C. Formation of Colloidal Copper Indium Sulfide Nanosheets by Two-Dimensional Self-Organization. *Chem. Mater.* **2017**, *29*, 10551−10560.

https://dx.doi.org/10.1021/acs.chemmater.0c02817
Chem. Mater. 2021, 33, 102−116